



Sedimentological and facies characterization in the modelling of the Turonian sandstone reservoir package, Jubilee field, Ghana

Ebenezer Ansah¹ · Anthony Ewusi² · Eric Thompson Brantson³ · Jerry S. Y. Kuma² · Saka A. Opeloye⁴ · Boadi K. Obeng⁵ · Clement Nuamah⁵

Received: 1 August 2022 / Accepted: 26 September 2022 / Published online: 8 October 2022
© The Author(s), under exclusive licence to Springer Nature Switzerland AG 2022

Abstract

Assessment of conditions that favoured hydrocarbon accumulations necessitates sedimentological characterization and facies identification as it elucidates the detailed records of the depositional environment and its evolution. Integration of various data sources becomes imperative for the establishment of the facies architecture which enables the evaluation of reservoir quality for Jubilee field in the deep Tano Basin. Early stage realization of decrease in production prediction of the field was attributed to early water breakthrough, baffle bridges and reservoir heterogeneity. This development requires its sedimentological evaluation through textural characterization, lithofacies identification and reservoir quality indication. The identified seventeen lithofacies allowed the deduction of deep-marine turbidite depositional environment. Our findings highlight the significance of sedimentological and facies development processes in the overall evolution of deep-water channel systems. The history of the Jubilee channel complex sets almost definitely characterizes many other emerging undersea channel systems and can be used to evaluate the distribution, shape, and structuring of the resulting reservoir sands. In turn, the Jubilee data set adds to the library of channel-levee-splay-lobe systems, aids as a prospective predictive model for hydrocarbon exploration and development, and as an outcrop explanatory analogue of a channel-splay system.

Keywords Sedimentological characterization · Jubilee field · Facies · Turbidite

Introduction

Sedimentological and facies characterization is critical for assessing the prerequisites that favoured hydrocarbon accumulation. The establishment of facies distribution in

reservoir architecture aids in perceiving reservoir heterogeneity for hydrocarbon field development. The studying of rock outcrops can provide full knowledge of the facies architecture and their quality (Martinius et al. 2013; Siddiqui et al. 2019, 2020). In the absence of outcrops, core sample, Gamma ray (GR) pattern and 3-D seismic volume are critical for understanding reservoir sandstone geometry, architecture, and quality, which are essential components for hydrocarbon field development and exploitation (Donselaar and Schmidt 2005; Farrell et al. 2013; Lowe et al. 2019; Radwan 2021; Omisore et al. 2022). Many researchers have used outcrops, core samples, and well logs to better understand sedimentary facies architecture at the regional and subsurface levels to estimate reservoir properties (e.g., Shukla 2009; Tullius et al. 2014; Siddiqui et al. 2020; Ali et al. 2021). The analysis of facies and establishing their paleoenvironment can also be based on descriptions of core samples in terms of sedimentary textures and elemental composition (e.g., Martinius et al. 2013; El-Tehiwy et al. 2019; Huang et al. 2020; Solórzano et al. 2021). The combination of these tools (outcrop, core

✉ Ebenezer Ansah
ansahessel@gmail.com

¹ Department of Petroleum Geosciences and Engineering, School of Petroleum Studies, University of Mines and Technology, Tarkwa, Ghana

² Department of Geological Engineering, Faculty of Geosciences and Environmental Studies, University of Mines and Technology, Tarkwa, Ghana

³ Department of Petroleum and Natural Gas Engineering, School of Petroleum Studies, University of Mines and Technology, Tarkwa, Ghana

⁴ Department of Applied Geology, Federal University of Technology Akure, Akure, Ondo State, Nigeria

⁵ Geophysics Department, Ghana National Petroleum Corporation, Tema, Ghana

data, well log, 3D seismic volume) can provide crucial insights into sand body thickness, shape, particle size distribution, lithology, and depositional environment. Integration of these tools has been used in sedimentological and facies modelling (e.g., Islam et al. 2017; Al-Mimar et al. 2018; Pacheco et al. 2019; Pattison 2019; Shahbazi et al. 2020; Ahmed 2021; Xu et al. 2022;) to understand reservoir sand distribution and its reservoir quality.

The Turonian clastics serve as the main reservoir in the Jubilee field, Ghana (Fig. 1) which is one of the most important producing areas within the Deep Tano contract Area. The Jubilee field in its early stage of production saw a decrease in production prediction, which was attributed to early water breakthrough, baffle bridges, increasing gas–oil ratio, inadequate pressure support and reservoir heterogeneity. Due to these factors, studies have described the stratigraphic blueprint for the Basin (Atta-Peters et al. 2013; Rüpke et al. 2010; Bempong et al. 2021a, b) to help address some of these problems but neither of the authors focused on the sedimentological and facies characterization modelling of the Jubilee reservoir. The current study, therefore, is an assessment of the reservoir characterization through textural analysis, facies interpretation and depositional modelling of the Jubilee Turonian reservoir.

The ensuing proposed depositional model will provide insight into the fields paleogeographic evolution, while the textural assessment of the reservoir architecture will aid in the evaluation of the flow behaviour. To achieve this purpose, the objective of the study is to (1) characterize the textural relationship of grain size distribution and their genetic significance, (2) create a lithofacies identification from core image, and (3) use a high-resolution 3D seismic volume of the subsurface to elegantly assist in revealing the depositional architecture of the reservoir. The outcome of the study will not only serve as a link within the Jubilee contract area but also by extrapolations be useful in the other parts of the basin thereby reducing the uncertainty of field development.

Geological setting

The study area is located south of the Deepwater Tano Basin (Fig. 1). Tano Basin is a coastal basin in Ghana's south-western region that is part of the West African Transform Margin basin family. It is bounded by a greater portion offshore and a lesser portion onshore. The basin is bounded to the north by the African mainland, to the west and east by St Paul and Romanche transform zones, and to the south by the ocean. It evolved as a pull-apart basin (Atta-Peters et al.

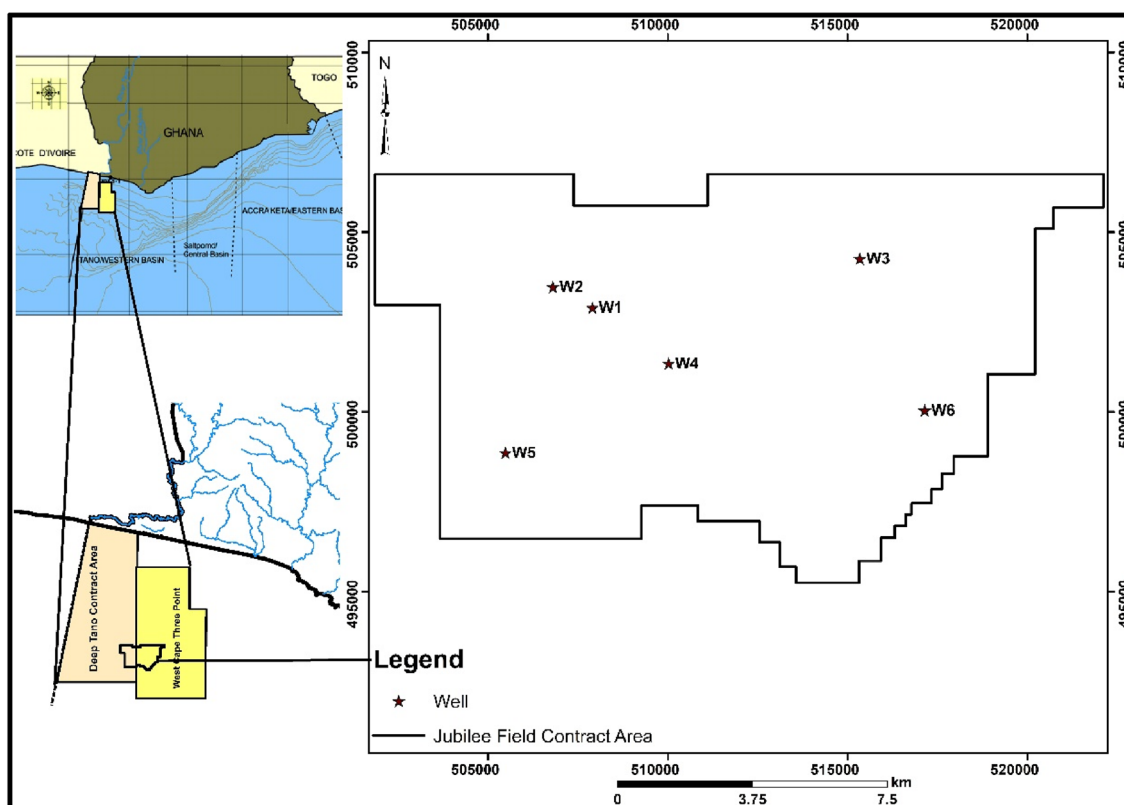


Fig. 1 Location map of the study area showing the wells used for the studies

2013) as a result of continental rifting during the Mesozoic Era. Subsequent extension and subsidence of the rift system's thinned continental crust and created space for lithic fill into the basin as the South Atlantic Ocean opened up and deepened (Bempong et al. 2021a). Wrench tectonics in the Cretaceous, on the other hand, alters the basin through a large-scale transform fault associated with sagging and fracture (Rüpke et al. 2010). The basin's lithic fill began in the Aptian, with significant continental clastic from rivers Tano and Ankroba (Bempong et al. 2021a). According to Dailly et al. (2013), the submarine canyon system served as a clastic sediment delivery system into the Tano Basin. The relationship between tectonic phases and associated sedimentation is defined by four patterns as enumerated below (Fig. 2):

1. The pre-rift phase of a stable platform was identified as Paleozoic to lower Mesozoic deposits.
2. The syn-rift phase, which began in the Jurassic and progressed to the Lower Cretaceous, was characterized by

a continental rifting between Africa and South America. The drifting forced the continental margin into a transpressional setting, which was recorded in the basin by a series of folds and flow structures. These records indicate that the continental margins played a role in the overall shearing between the two plates.

3. The top syn-rift unconformity, denotes the end of a period of intense continental rifting and deformation. It is distinguished by a noticeable angular unconformity across the continental platform, as evidenced by a Top Syn-rift reflection on the seismic profile. The unconformity corresponds to the last continental contact between the two plates, which occurred near the end of Albian or early Cenomanian. According to Antobreh et al. (2009), the episode of thermal uplifting of the outer Ghana margins at the end of the Albian is plausible to coincide with magnetic underplating reported in deep seismic gravity and magnetic records across the margin Rüpke et al. (2010).

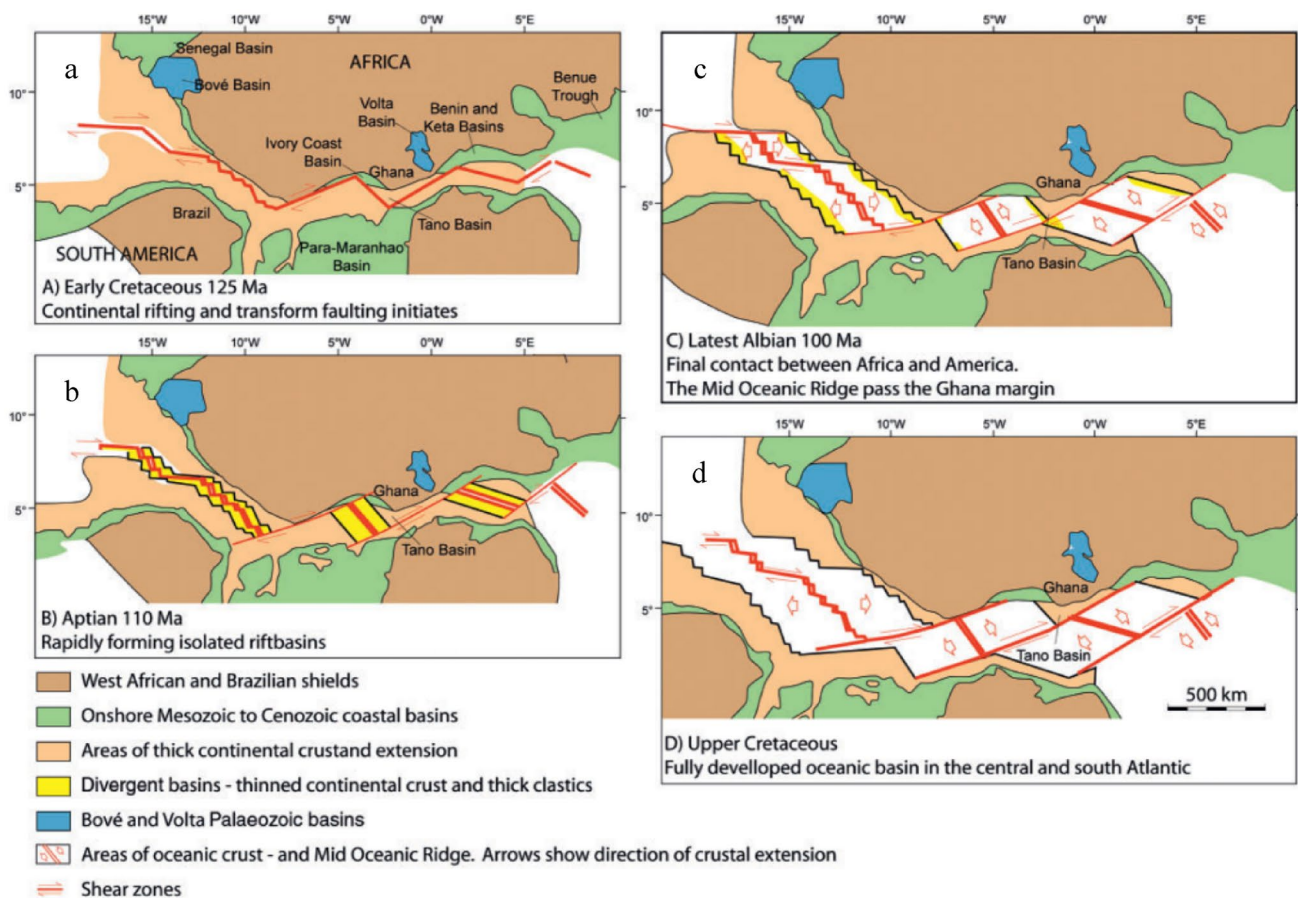


Fig. 2 Paleogeological setting during the tectonic phase of the breakup of Africa and South America (Rüpke et al., 2010). **a** Early Cretaceous 125 Ma, continental rifting and transform faulting initiation, **b** Aptian 110 Ma, rapidly forming isolated rift basins, **c** latest

Albian 100 Ma, final contact between Africa and America, and **d** Upper Cretaceous, fully developed oceanic basin in the central and south Atlantic

4. The post-rift phase denotes marine sedimentation from the Cenomanian to the recent, which occurred following the final breakup of the American and African plates. Full-scale ocean transform faults (St Paul and Romanche transform) developed along the trace of the older continental transforms during this phase (Fig. 2). Although some deformation may have continued into the continental margins, the final break up generally marks a period of rapid subsidence and thermal subsidence.

Reservoir zonation

The Jubilee field has two main reservoir intervals: the Upper and Lower Mahogany. The intervals are separated by extensive regional shale section (Table 1). The lower Mahogany is classified into LM4 to LM1 in succession and overlain by shale, while the Upper Mahogany is classified as UM4 to UM1 in succession. Of all these successions of sandstone bodies, the volumetrically significant are LM2A and LM2B which are denoted as MH1 (seismic stratigraphic section), as well as UM3A to C, denoted as MH4 (on the seismic stratigraphic section), as indicated in Fig. 3. The two reservoirs were considered with several producers and injector wells in the initial development program.

Materials and methods

The study derives from exploration, appraisal and development wells from the Jubilee field, Ghana that penetrated through the Turonian reservoir (from LM3 to MH5 of the

Lower and Upper Mahogany). A total number of six well log suits is involved and are denoted as W1 to W6. Three of the wells have core data (i.e., W1 to W3), while W2 and W3 are employed for petrographic assessment. Since this study is focused on the volumetrically significant reservoirs of MH1 and MH4, penetrations of wells into other reservoirs only serve as complementary information for improving the knowledge of sand quality and fluid distribution.

The workflow for this study includes petrographic observation, lithotype/lithofacies determination, depositional package identification and modelling of the depositional setting (Fig. 4). Core images are used for lithofacies identification and reservoir quality assessment. Gamma ray log is eventually employed for facies correlation and upscaling the lithofacies to bed-stack facies association. Sieve analysis data allowed for the determination of textural characteristics using statistical grain size parameters based on calculations of Ghaznavi et al. (2019). Bivariate plots of the textural parameters as well as Linear Discriminate functions (Eqs. 1–4) (Ghaznavi et al. 2019) are used to interpret the depositional environment with the equation below;

$$Z_{1Aeol:Beach} = -35688M + 3.7013SD^2 - 2.0766SK + 3.1135K \tag{1}$$

For a beach subenvironment (B), $Z_1 > -2.741$, while $Z_1 < -2.7411$ represent aeolin environment (Ae)

$$Z_{2Beach:Shallowmarine} = 15.653M + 65.7091SD^2 - 18.1071SK + 18.5043K \tag{2}$$

Table 1 Turonian reservoir zonation of the Jubilee field

Series/epoch	Stage/age	Reservoir classification	Seismic stratigraphy reservoir zonation	Wireline log reservoir zonation		
Mid-Cretaceous	Coniacian	Upper Mahogany	MH5	UM1		
				UM2		
	Turonian		MH4	UM3A		
				UM3B		
				UM3C		
				UM4		
				Lower Mahogany	Middle Shale	LM1
						LM2A
	Cenomanian		Pre-Mahogany	LM3	LM2B	
					LM4	

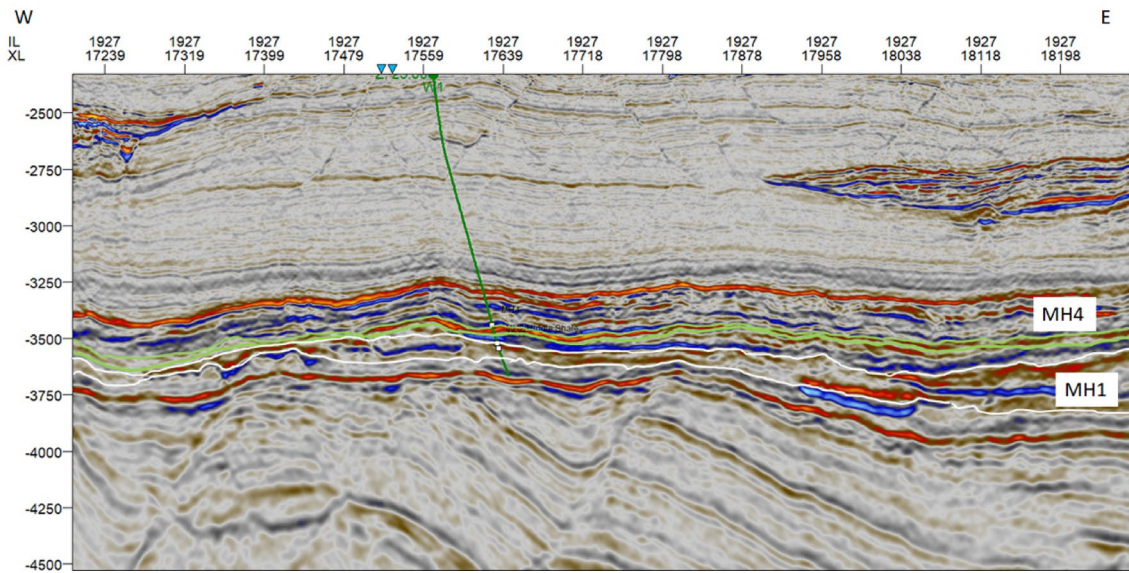
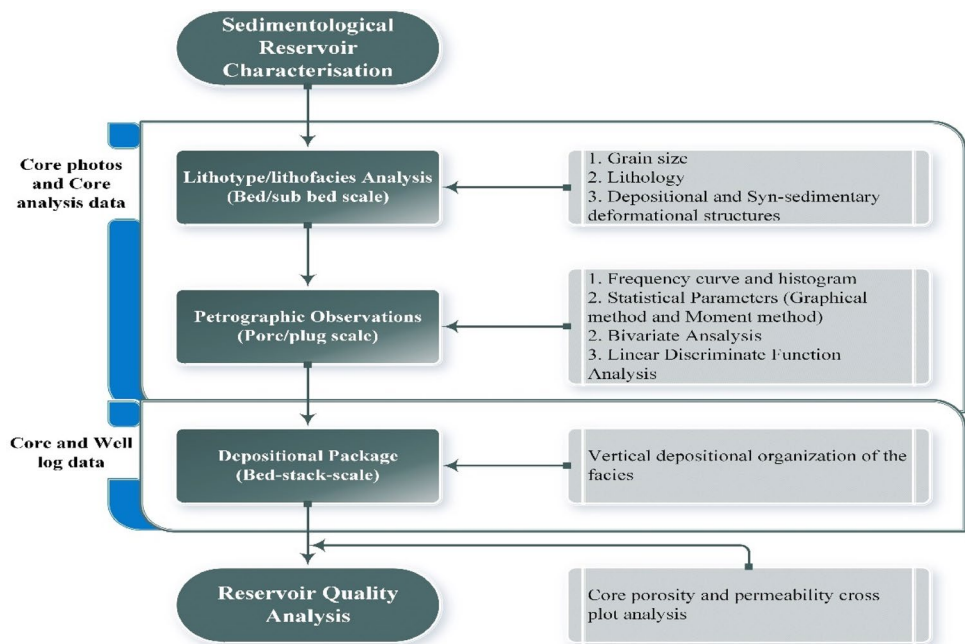


Fig. 3 Seismic depth section of MH1 (green) and MH4 (white) reservoir section through selected well of the Jubilee field

Fig. 4 Flowchart adopted for the work



$Z_2 < 63.3650$ for the beach subenvironment (B), while $Z_2 > 63.3650$ for the shallow-marine subenvironment (SM).

$$Z_{3\text{Shallowmarine:Fluvial}} = 0.2852M - 8.7604SD^2 - 4.8932SK + 0.0428K \quad (3)$$

$Z_3 > -7.4190$ for the shallow-marine subenvironment (SM), whereas $Z_3 < -7.419$ for the Fluvial subenvironment (F).

$$Z_{4\text{Fluvial:Turbidity}} = 0.7215M + 0.403SD^2 + 6.7322SK + 5.2927K \quad (4)$$

$Z_4 > 10$ denotes the marine turbidity subenvironment (T), while $Z_4 < 10$ represents the fluvial subenvironment (F).

Results

Petrographic properties of the sandstone samples

Frequency curve and histogram

Peak constituents and consistency of sediment fractions for the study area are depicted by frequency distribution curves from the two wells (W2 and W3). Figure 5 represents the assemblage of the descriptive statistical curves for the two wells. The frequency distribution on the frequency curves is unimodal (Fig. 5a–g) and bimodal (Fig. 5h). The curves' unimodality is due to less variation in the depositional velocity and a constant depositional process over which sediment settled (Boggs 2012). The assertive peak in the bimodal distribution was at 3 phi, and the passive peak was at 7 phi (Fig. 5h). The fine and silt components of the bimodal grain-size distribution could be attributed to several depositional processes and/or mixing of different size populations from the source area. Bimodality can also be attributed to the low energy of the transporting medium and the difference in modes of transportation. The histogram (Fig. 5a–h) revealed a range of very fine to medium sand, with a low percentage of the very coarse-grained sand present only in conglomerate samples.

Furthermore, phi values are plotted against cumulative frequencies, indicating an impact of different mechanisms of sediment supply and deposition in the formation of sandstone units. When plotted on an arithmetic scale, the curve typically exhibits an S-shaped trend (Fig. 5–h). Results for the cumulative percentage curve indicate many sediment transport and deposition were attributed to saltation, passive suspension, and minor traction (Fig. 5a–h). The slope of the middle portion of the curve can predict sorting (Ghaznavi et al. 2019). A broad and gentle slope indicates low kinetic energy and velocity, indicating poor sorting (Fig. 5a, c and h). A very steep slope, on the other hand, indicates good sorting (Fig. 5d–g). On the cumulative percentage plot, the value of phi ranges from 0 to 4 phi, with most curves exhibiting an almost identical broad and gentle slope S-shaped trend (Fig. 5). As a result, they can be reliably classified as fine to medium-grained (e.g., Spencer 1963; Ghaznavi et al. 2019; Siddiqui et al. 2020). The gentle slope indicates that such grains have been very poorly sorted (Fig. 5).

Statistical parameters—graphical method

Graphical mean: the graphical mean ranges from 1.12 to 10.34, with an average of 3.53 (Table 2). The average

mean of the reservoir unit denotes fine-grained sand sediments. The distinct nature of the size distribution with fine sand may be attributed to the low-energy environment that existed during deposition (Ghaznavi et al. 2019). The values of certain sand samples, such as Sb, Sf, Sm, and Sxr, are quite high due to the dominance of a particular mode of sediment class (Fig. 6a). However, a few sample values, such as Cgl, Sc, and Sd, are low due to a nearly equal proportion of coarse and fine sediments, as indicated in Fig. 6a and Table 2. It is a poorly sorted type due to the wide variation in grain size.

Phi standard deviation: the kinetic energy variation associated with the mode of deposition concerning the particle size distribution is represented by the standard deviation. The standard deviation is an important parameter in sediment analysis, because it reflects the energy situation of the depositional environment (Ghaznavi et al. 2019), but it does not primarily assess the quality to which the sediment has been blended. The reservoir units' phi standard deviation ranges from 1.03 to 6.58 phi, with an average of 2.50 phi, indicating that the sediments are very poorly sorted (Fig. 6b, Table 2). The poorly sorted nature of the sediment depicts a blending of sediments of various sizes. The poorly sorted samples indicate that the current velocity of the transporting media varies slightly (Fig. 6b).

Graphic skewness: skewness is a measure of sediment distribution symmetry. Skewness is useful in environmental forecasting, because it is proportional to the fine and coarse tails of particle size and thus indicative of deposition energy. For the sand samples, the skewness values range from 0.26 to 0.57 phi, with an average skewness of 0.35 phi indicating finely skewed or positive skewness (Fig. 6c, Table 2). The positive skewness suggests that population growth is taking place in a low-energy environment (Fig. 6c). The fine tail of the sediments contains a higher concentration of material.

Graphic kurtosis: the samples peak from 1.31 to 2.74, with an average of 1.62 (Table 2). The vast majority of grains are leptokurtic, with a few notable exceptions that are extremely leptokurtic (Fig. 6d). This demonstrates that the tails portion is usually sorted equally.

Statistical parameters—moment measures method

1st moment—mean: the graphic mean ranges from 0.97 to 2.17, with an average of 1.47 (Table 3), indicating medium grain size. Only two samples, Sx and Sxr, are coarse and fine-grained, respectively; the rest have a medium-grained texture (Fig. 7a).

2nd moment—standard deviation: this metric measures grain sorting or uniformity, indicating the energy conditions that existed during transport and deposition. Its value ranges from 0.76 to 1.18, with a mean of 1.05 (Table 3).

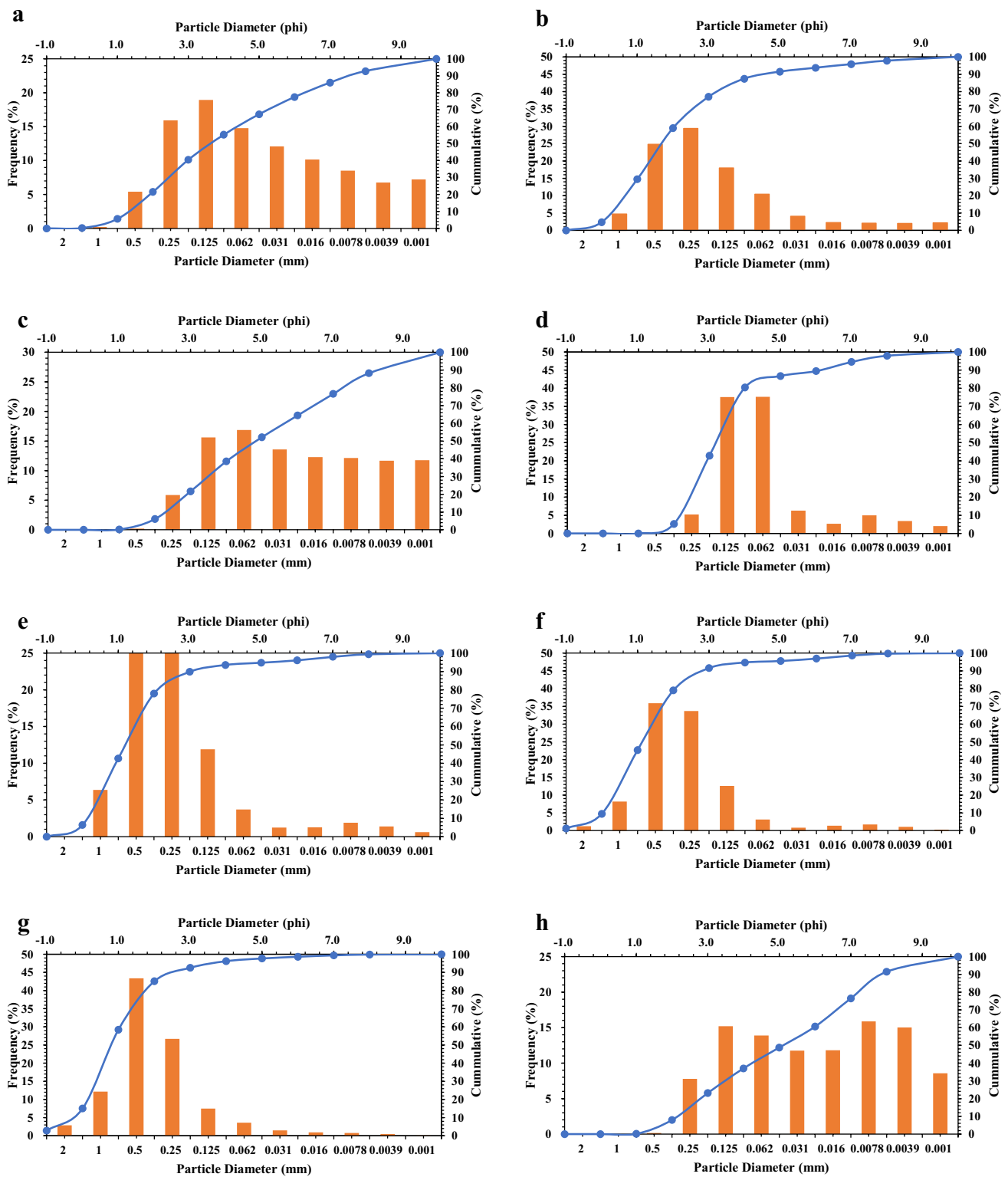


Fig. 5 Grain size distribution and cumulative frequency curve for some sandstone facies for the Turonian reservoir unit; **a** unimodal histogram for Sd; **b** unimodal histogram for Ss; **c** unimodal histogram

for Sc; **d** unimodal histogram for Sxr; **e** unimodal histogram for Sp; **f** unimodal histogram for Sm; **g** unimodal histogram for Cgl and **h** bimodal histogram for Sc

Table 2 Graphical statistical parameters of the grain size distribution for the Mahogany reservoir sandstones of the Jubilee field, calculated in phi units

Facies	Mean	Standard deviation	Skewness	Kurtosis
Cgl	1.12	1.40	0.29	1.49
Sb	2.75	1.44	0.37	1.66
Sc	1.42	1.50	0.26	1.37
Sd	1.84	1.64	0.27	1.34
Sf	3.04	1.58	0.42	2.74
Sm	6.55	5.37	0.37	1.59
Sp	2.27	1.30	0.32	1.45
Ss	2.42	1.65	0.27	1.31
Sxr	10.34	6.58	0.57	1.66

Ultimately, the samples show poor sediment sorting, with only two samples, Sm and Sx, showing moderate sorting (Fig. 7b).

3rd moment—skewness: the skewness ranges from 0.72 to 2.45, with an average of 1.89 (Table 3). All samples are very finely skewed (Fig. 7c), indicating a population accumulation in a low-energy environment.

4th moment—kurtosis: Kurtosis values range from 3.78 to 10.52, with an average of 6.61. All of the samples are of the leptokurtic type (Fig. 7d), with equal sorting in the tails.

Bivariate grain size parameter

Multiple bivariate analysis seeks to evaluate a wide range of data analyses, which aids in clearly determining the depositional environment (Ghaznavi et al. 2019). According to Moiola and Weiser (1968) and Azidane et al. (2021), bivariate is most effective in distinguishing between the beach and river sands, as well as river and coastal dune sands, and the distinction works well whether quarter, half or whole phi data are used. Bivariate plots are used by Friedman (1961), Moiola and Weiser (1968) and Tan et al. (2019) to distinguish between the river, coastal dune, and beach subenvironments. Therefore, to confirm the current paleoenvironmental conditions, statistical properties derived using both graphical and moment techniques were plotted in various bivariate diagrams. To distinguish between the beach and river sedimentary subenvironments, Friedman (1961, 1967), Rajganapathi et al. (2013) and Su et al. (2021) developed a bivariate by plotting skewness vs. standard deviation. The sample points are all drawn to the river environment (Fig. 8a). The bivariate plot between kurtosis and skewness (e.g., Folk and Ward 1957; Rajganapathi et al. 2013 and Ghaznavi et al. 2019) was used to further distinguish between coastal areas, dune environments, and fluvial environments which confirmed that of Friedman (1961, 1967) bivariate plot. In the case of both the graphical and moment method, all samples represent that of a fluvial environment (Fig. 8b). The bivariate

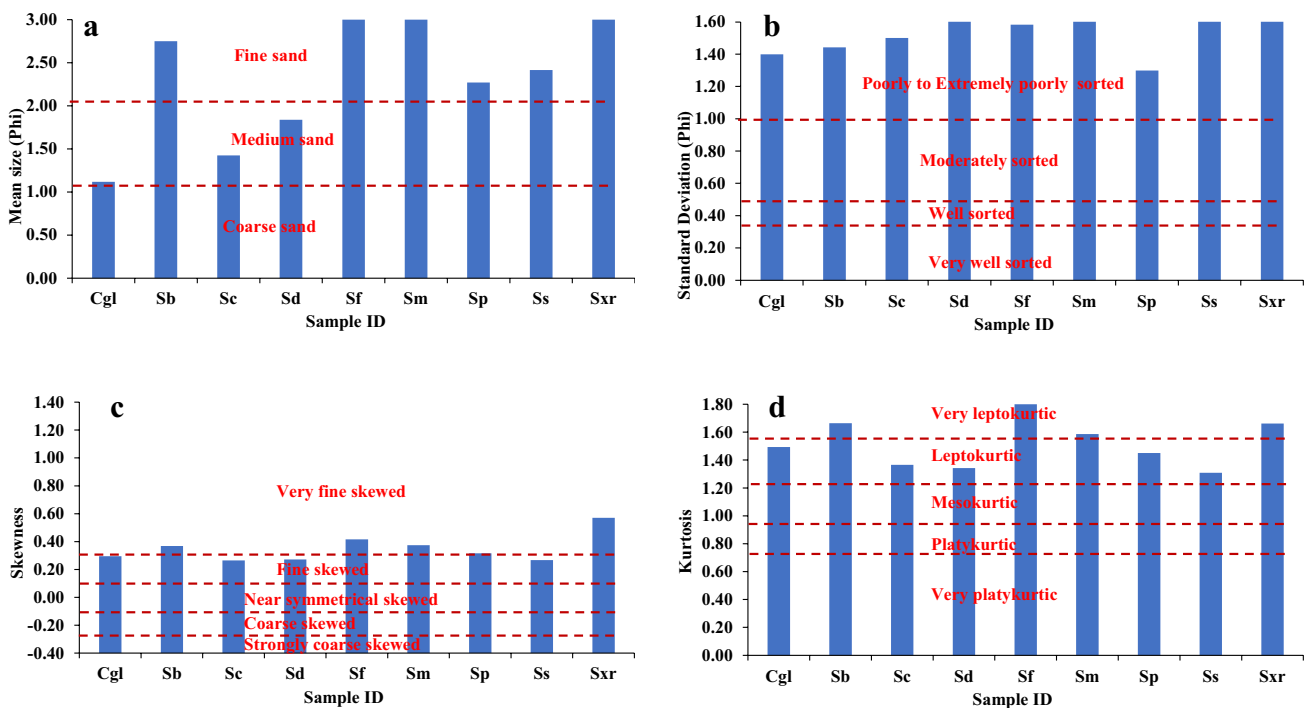


Fig. 6 Histograms of all samples plotted with respect to statistical parameters calculated by the graphical method: **a** mean grain size; **b** standard deviation; **c** skewness and **d** kurtosis

Table 3 Graphical statistical parameters of the grain size distribution for the Mahogany reservoir sandstones of the Jubilee field, calculated by the moment method

Facies	1st moment mean	2nd moment standard deviation	3rd moment skewness	4th moment kurtosis
Cgl	1.35	1.10	2.30	6.53
Sb	1.54	1.04	2.36	7.03
Sc	1.31	1.06	1.93	6.24
Sd	1.39	1.04	1.66	5.77
Sf	1.88	1.01	2.45	7.22
Sm	1.09	0.94	1.79	7.12
Sp	1.48	1.18	1.66	6.11
Ss	1.53	1.16	1.64	5.82
Sx	0.97	0.76	2.39	10.52
Sxr	2.17	1.18	0.72	3.78

plot reveals that all of the samples are from the fluvial sub-environment (Fig. 8a, b).

Linear discrimination function analysis

Based on the results of the linear discriminate function using statistical parameters obtained by the graphical method, it was discovered that Z_1 indicated that all samples belonged to the beach subenvironment (Table 4 and Fig. 9a). The

Z_2 values indicate that the sediments are shallow-marine (Table 4 and Fig. 9b). In a comparison of fluvial and shallow-marine dominance using Z_3 , the former prevailed over the latter (Table 4 and Fig. 9c). Z_4 shows that the sediments were deposited primarily by fluvial action, with turbidity action being a component of both the turbidity and fluvial processes (Table 4 and Fig. 9c).

When the statistical parameters were used, there was no difference between the LDF calculated using the moment method and the LDF calculated using the graphical method.

Thin section analysis

The petrographic analysis of the conventional core samples from the three wells is presented in this section. The following are the photomicrograph and description details for the reservoir sandstones:

Burrowed sandstone (Sb)

Sb is constituent by abundant monocrystalline quartz (white) framework grain, with less plagioclase (PF) and polycrystalline quartz (PQ) (Fig. 10a). The most common type of matrix contains only a small amount of syntaxial quartz overgrowths (qo). This poorly sorted sandstone has a medium grain size. Due to trace amounts of authigenic clays

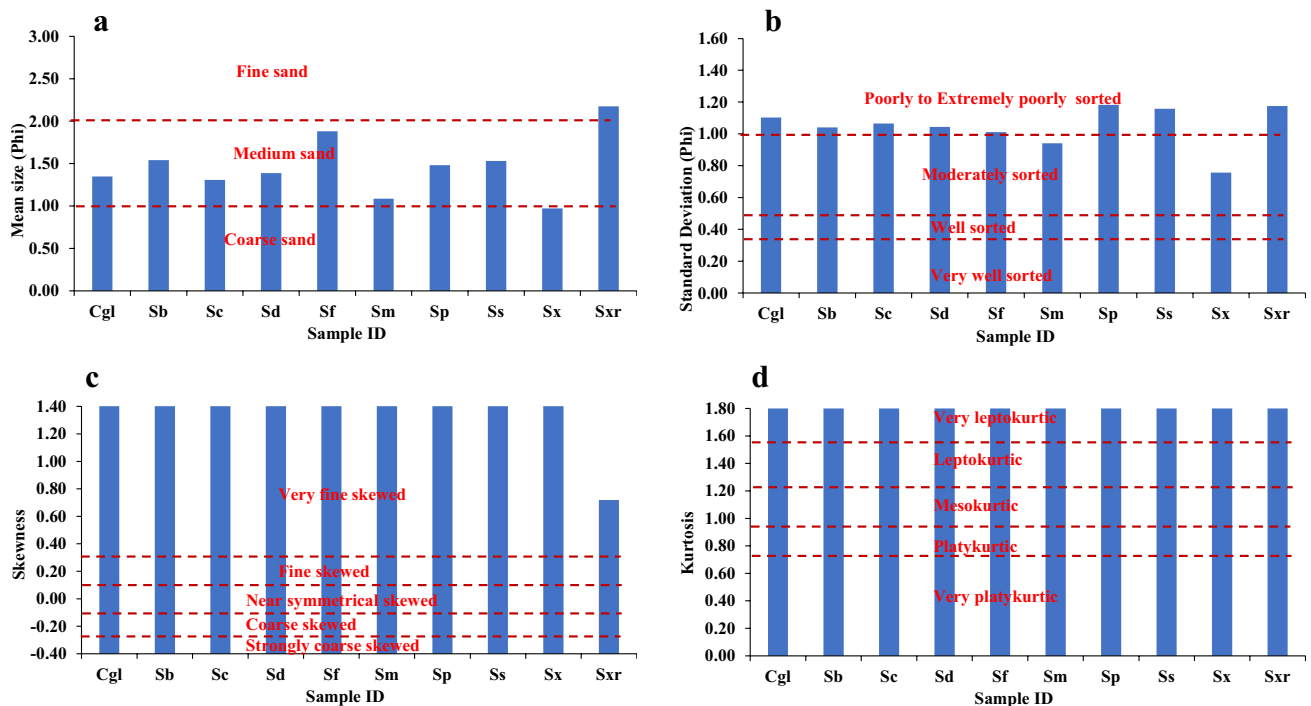


Fig. 7 Histograms of all samples plotted with respect to statistical parameters calculated by the moment method: **A** mean grain size; **B** standard deviation; **C** skewness and **D** kurtosis

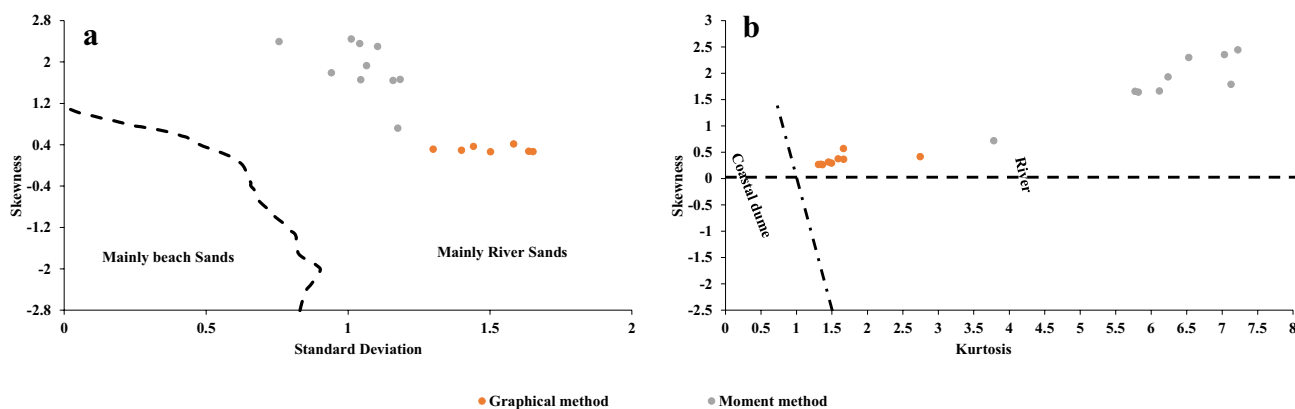


Fig. 8 **a** Bivariate plot of skewness against inclusive graphic standard deviation (after Friedman, 1967) and **b** bivariate plot of skewness against kurtosis (after Folk & Ward, 1957)

Table 4 Linear discriminate function analysis to interpret variation in energy and fluidity factors using the graphical method

Facies	Z ₁	Env	Z ₂	Env	Z ₃	Env	Z ₄	Env
Cgl	7.29	B	179.15	SM	- 18.21	F	11.48	T
Sb	2.30	B	217.07	SM	- 19.15	F	14.11	T
Sc	6.96	B	200.49	SM	- 20.58	F	10.95	T
Sd	6.97	B	234.61	SM	- 24.22	F	11.34	T
Sf	6.10	B	270.61	SM	- 23.01	F	20.52	T
Sm	87.63	B	2035.35	SM	- 252.76	F	27.27	T
Sp	2.01	B	179.02	SM	- 15.63	F	12.12	T
Ss	4.99	B	246.06	SM	- 12.45	F	11.57	T
Sxr	127.41	B	3048.66	SM	- 379.17	F	37.55	T

in this sandstone, the intergranular pores (Pi) are large and appear to be well-interconnected (Fig. 10b).

Scanning electron microscopy (SEM) analysis revealed the presence of qo, which reduces intergranular pore sizes in this sandstone (Fig. 10c). Patches of localized authigenic kaolinite (kao) were also present, but no authigenic chlorite was detected (Fig. 10d).

Pebbly sandstone (Sc)

As shown in Fig. 11a, the maximum framework of this poorly sorted coarse-grained sandstone is composed of monocrystalline quartz (white) and polycrystalline quartz (PQ; also, white). As shown in Fig. 11b, this sandstone contains minor amounts of qo. Some authigenic chlorite (cl) linings and trace amounts of kao are present in isolated patches. In this sandstone, Pi appears to be well-interconnected. This cl lines the intergranular pore in this sandstone, according to SEM analysis (Fig. 11c).

Figure 11d depicts minor amounts of discontinuous qo coating a detrital quartz grain. This sandstone also contains trace fibres of authigenic illite (I) (Fig. 11d).

Fine-grained sandstone (Sf)

Sf is primarily composed of monocrystalline quartz (mostly white grains) and minor amounts of plagioclase (PF). On quartz grains, moderate amounts of qo cement are observed, with kao being the most common authigenic clay recorded (Fig. 12a). As shown in Fig. 12b, three types of macropores have been identified: intergranular, secondary intragranular, and grain moldic. Pi is the most numerous and appears to be well-interconnected. Secondary intragranular pores (Ps) are small, isolated pores found mostly in feldspars (Table 5).

In the SEM analysis, intergranular pores are highlighted in Fig. 12c. Figure 12d depicts an intergranular pore that has been reduced by qo. Intergranular areas are also occupied by booklets of kao. Authigenic chlorite traces coat portions of grains and appears to have formed before quartz cement.

Planar stratified sandstone (Sp)

The Sp is composed of medium-grained sandstone with poor grain size sorting. As shown in Fig. 13a, the framework grains are abundant monocrystalline quartz (white). Figure 13b depicts the authigenic minerals present, which

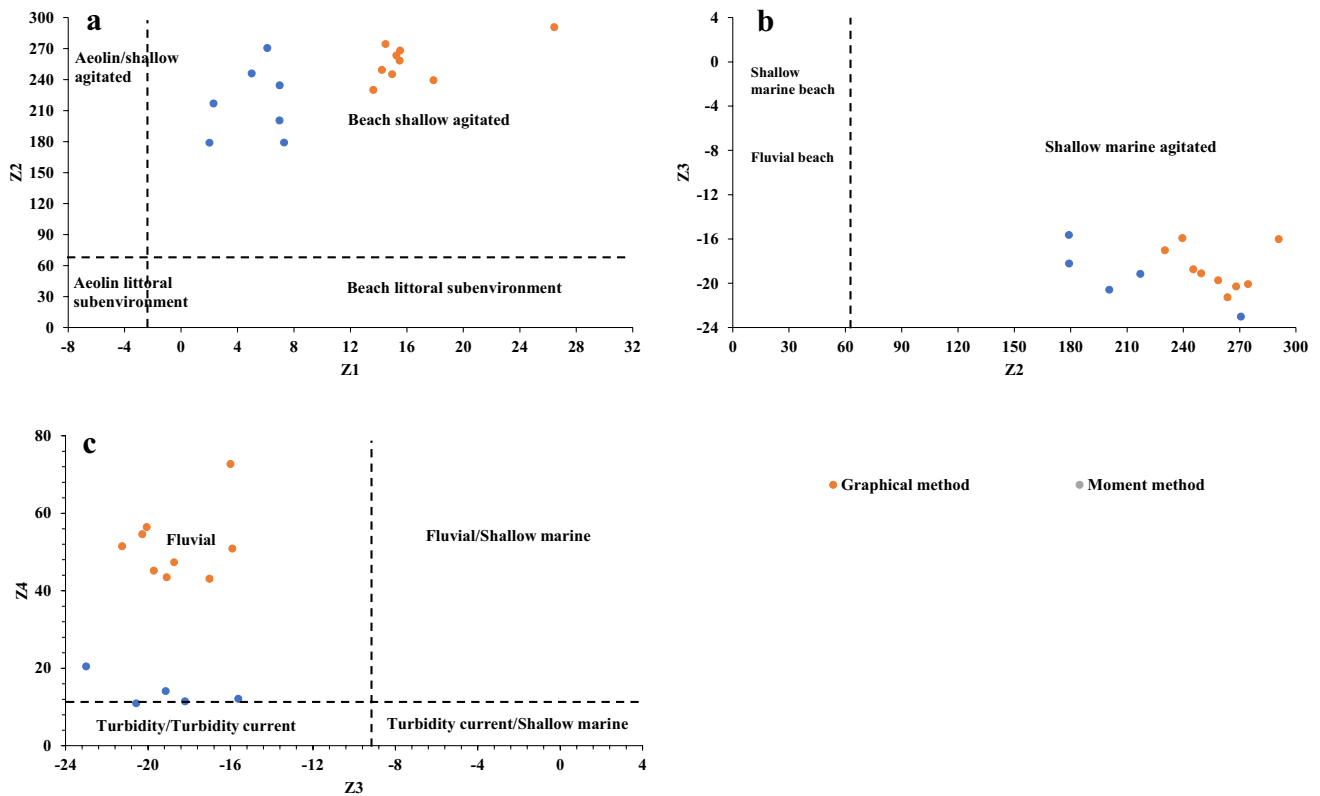


Fig. 9 Linear discriminate function plot for Turonian sandstones. **a** Z₁ vs. Z₂ discriminates between the beach and aeolian environment; **b** Z₂ vs. Z₃ discriminates between the beach and shallow-marine sub-

environment; **c** Z₃ vs. Z₄ discriminates between marine turbidity and fluvial environment

include cl, qo, and patchy kao. Primary intergranular, grain-moldic (Pm), and intercrystal pores are the three most common pore types found in chlorite and kaolinite authigenic clays.

Because of the abundance of authigenic minerals, intergranular pores (red arrows in Fig. 13c) are relatively small. The high-magnification view (Fig. 13d) shows authigenic cl coating grains and qo that appear to have formed after the cl.

Structureless sandstone (Ss)

Granule-sized grains coexist with sand-sized grains in this sandstone. The majority of the grains are monocry-stalline quartz (mostly white grains), with minor amounts of polycrystalline quartz (PQ) and plagioclase grains (PF) (Fig. 14a). Figure 14b depicts authigenic constituents, such as qo, kao, and cl, as well as trace amounts of authigenic pyrite (py). The most common macropore type observed is well-interconnected Pi.

Primary intergranular pores (red arrows) are visible in the photomicrograph as a result of the SEM analysis (Fig. 14c). Quartz overgrowth cement has reduced some of these pores. Pore-filling authigenic clays shown in the photomicrograph (Fig. 14d) include kao booklets and cl blades.

Conglomerate (Cgl)

This sandy conglomerate is poorly sorted. The majority of framework grains are monocry-stalline (most white grains) and polycrystalline (PQ) quartz, with minor feldspar grains. Mollusk fragments (Mol, stained red) are present in trace amounts (Fig. 15a). The most noticeable authigenic component is qo cement; authigenic clays such as kao are minor to rare (Fig. 15b). The most common pore type is well-inter-connected Pi.

Intergranular pores are highlighted in Fig. 15c as a result of the SEM analysis (arrows). Figure 15d shows qo, kao, cl, and py as the authigenic constituents present in this sample.

Ripple cross-laminated sandstone (Sxr)

Even though quartz constitutes the majority of the frame-work grains in these facies, the proportion of plagioclase (PF) in this sample is higher than in shallower samples (Fig. 16a). Quartz overgrowths are the most common inter-granular cement, with minor amounts of authigenic kao and trace amounts of chlorite also filling some pores (Fig. 16b). Primary intergranular pores are the most common pore type;

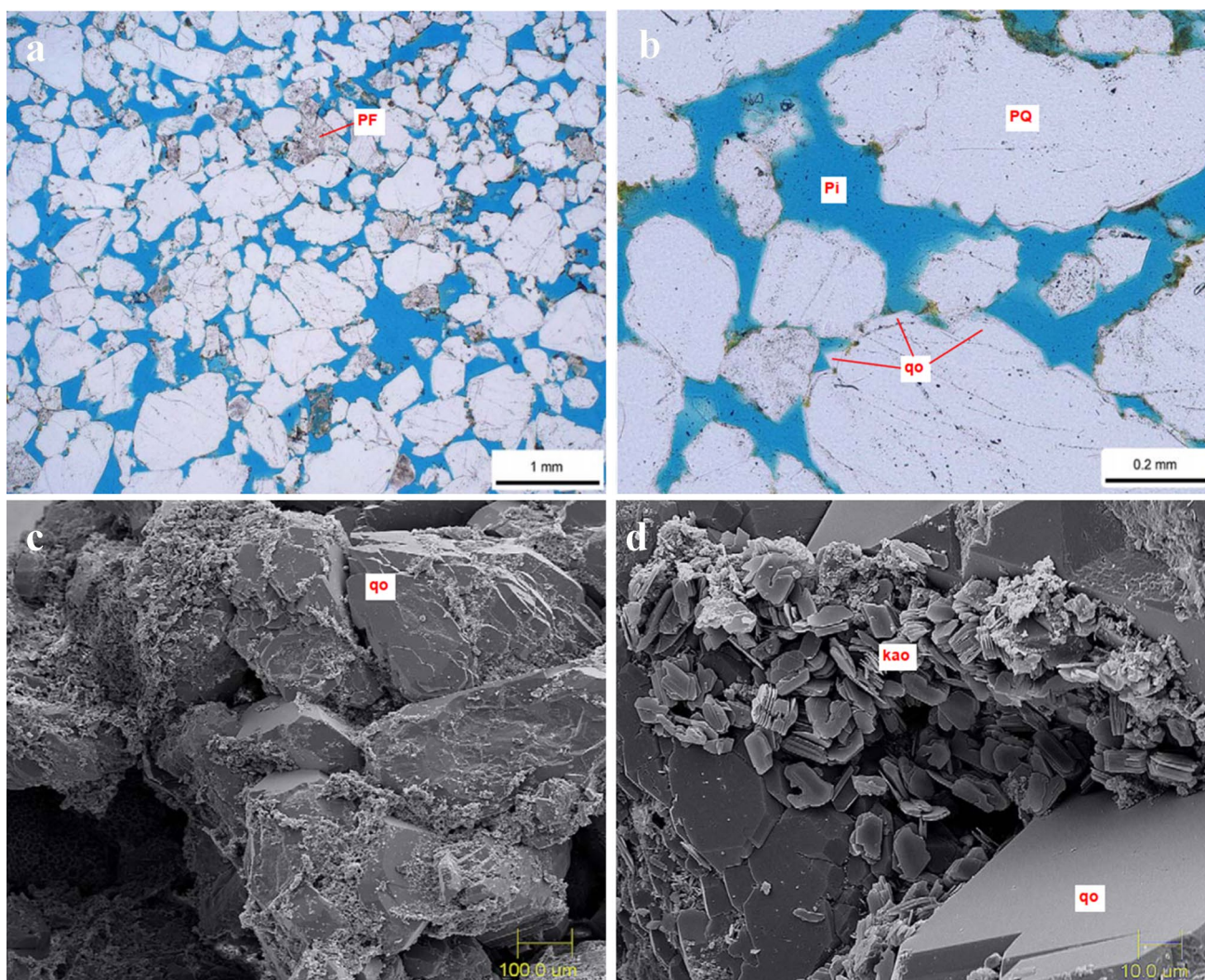


Fig. 10 **a, b** Photomicrograph of burrowed sandstone sample at 1 mm and 0.2 mm, respectively; **c, d** SEM photomicrography at 100 μm and 10 μm , respectively

secondary intragranular pores and grain-moldic pores are minor.

Because of the average grain size and qo cement, the intergranular pores (arrows) present are relatively small, as shown in Fig. 16c. Figure 16d depicts a minor patch of authigenic kao and trace amounts of bladed grain-coating cl partially filling some intergranular areas.

Sedimentary facies

The cored succession comprises thick intervals of sandstones and conglomerates interbedded with intervals of mudstones and heteroliths. These lithologies have been divided into sixteen depositional lithofacies, based on grain size, lithology, depositional and syndepositional deformational structures. Detailed descriptions of the characteristic features of the lithofacies are discussed below and summarized

in Table 6 with a coding scheme adopted by Ghana National Petroleum Commission (GNPC). The bed-stack facies for the cored wells are presented in Fig. 23.

Facies A: conglomerate

The conglomerate unit observed in the core units composed more than 50% clasts with a mud-poor sandy matrix. The conglomerate facies observed can be divided into two (2) subfacies. These are identified as: (1) conglomerate composed largely of extrabasinal clast (Fig. 17a) and (2) Conglomerate composed largely of mudstone clast (Fig. 17a).

Extrabasinal clast-conglomerate is composed of 40–60% granules to small pebbles of lithified sedimentary, igneous, or metamorphic rock in a sandstone matrix (Fig. 17a). W1 contains several beds of the extrabasinal clast-conglomerate

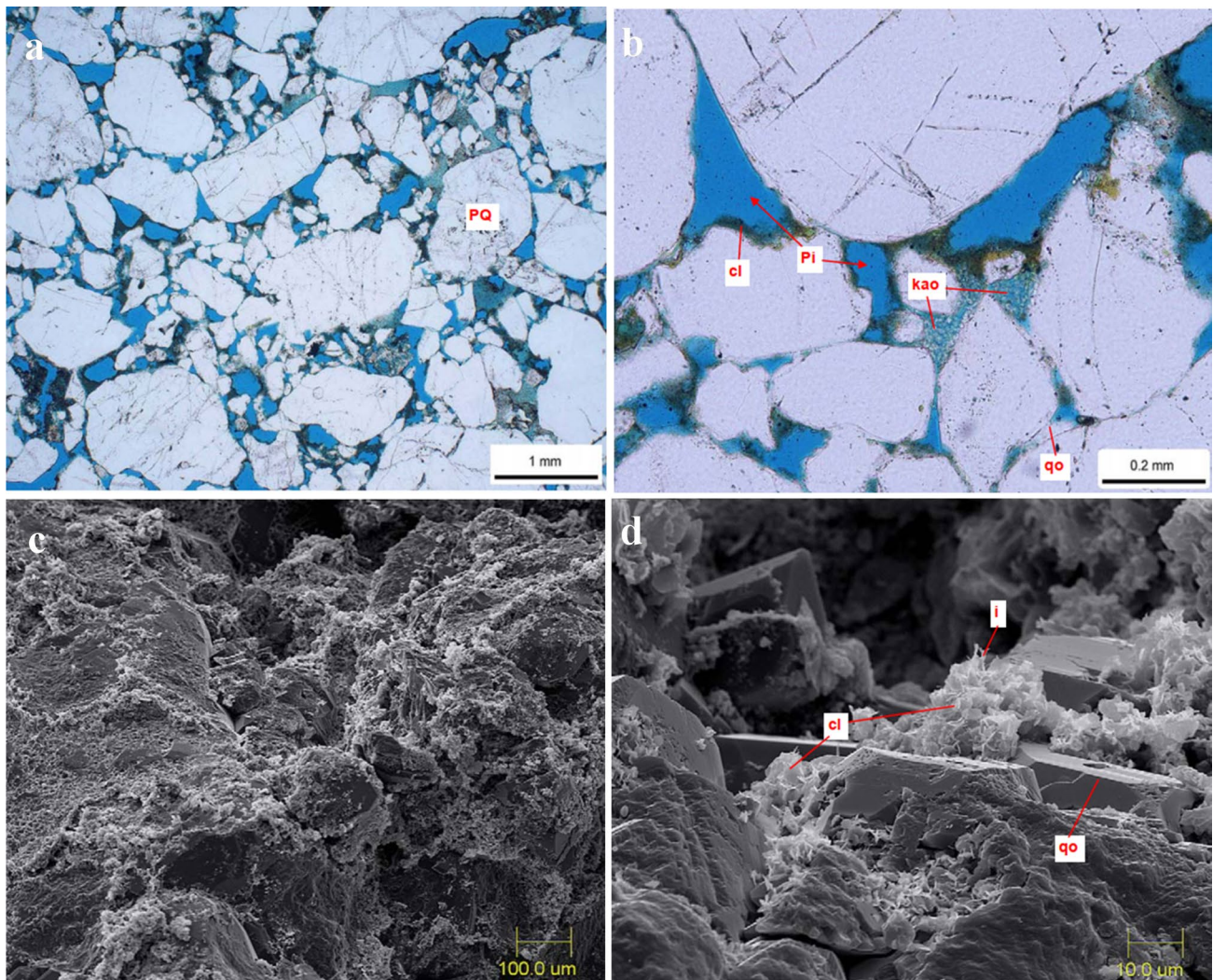


Fig. 11 **a, b** Photomicrograph of pebbly sandstone sample at 1 mm and 0.2 mm, respectively; **c, d** SEM photomicrography at 100 μm and 10 μm , respectively

(Fig. 17a). Similar beds can be found in minor components of the W2 and W3 core.

The mud-clast conglomerate is composed of angular clasts of dark gray mudstone in a sandstone matrix (Fig. 17b). These units represent grains transported within sandy high-density turbidity currents. W3 contains several beds made up of granule- to small-pebble-sized mud clasts embedded in a sandstone matrix (Fig. 17b). Similar beds can be found in minor components of the W1 core. These units are typically thin (1 m) with small clasts. These have been included in either the thick-bedded sandstone or the interbedded thick-bedded sandstone and thin-bedded sandstone and mudstone lithofacies on the graphic logs (Fig. 17c).

Conglomerate occurs mostly within thick-bedded sandstone units in the cores and occurs as S3 divisions of Lowe (1982) deposited by the collapse of dense floating clasts and sand high-density currents. Current structured sandstone

units are largely devoid of mud clasts, implying that they could not withstand abrasion and shearing during transport.

Facies B: sandstone

Facies B consists of more than 80% sandstone in beds that are mostly greater than 50 (cm) thick (Fig. 18). In general, the sandstone facies can be recognized as (1) Thick-bedded sandstone composed largely of sandstone beds deposited by high-density turbidity currents; structureless or showing water-escape structures (Fig. 18a); (2) Thick-bedded sandstone composed largely of current-structured sandstone deposited by low-density turbidity currents; dominated by Tb and Tc Bouma divisions (Fig. 18b); (3) Medium-bedded sandstone (Fig. 19), and (4) Thin bedded sandstone (Fig. 20).

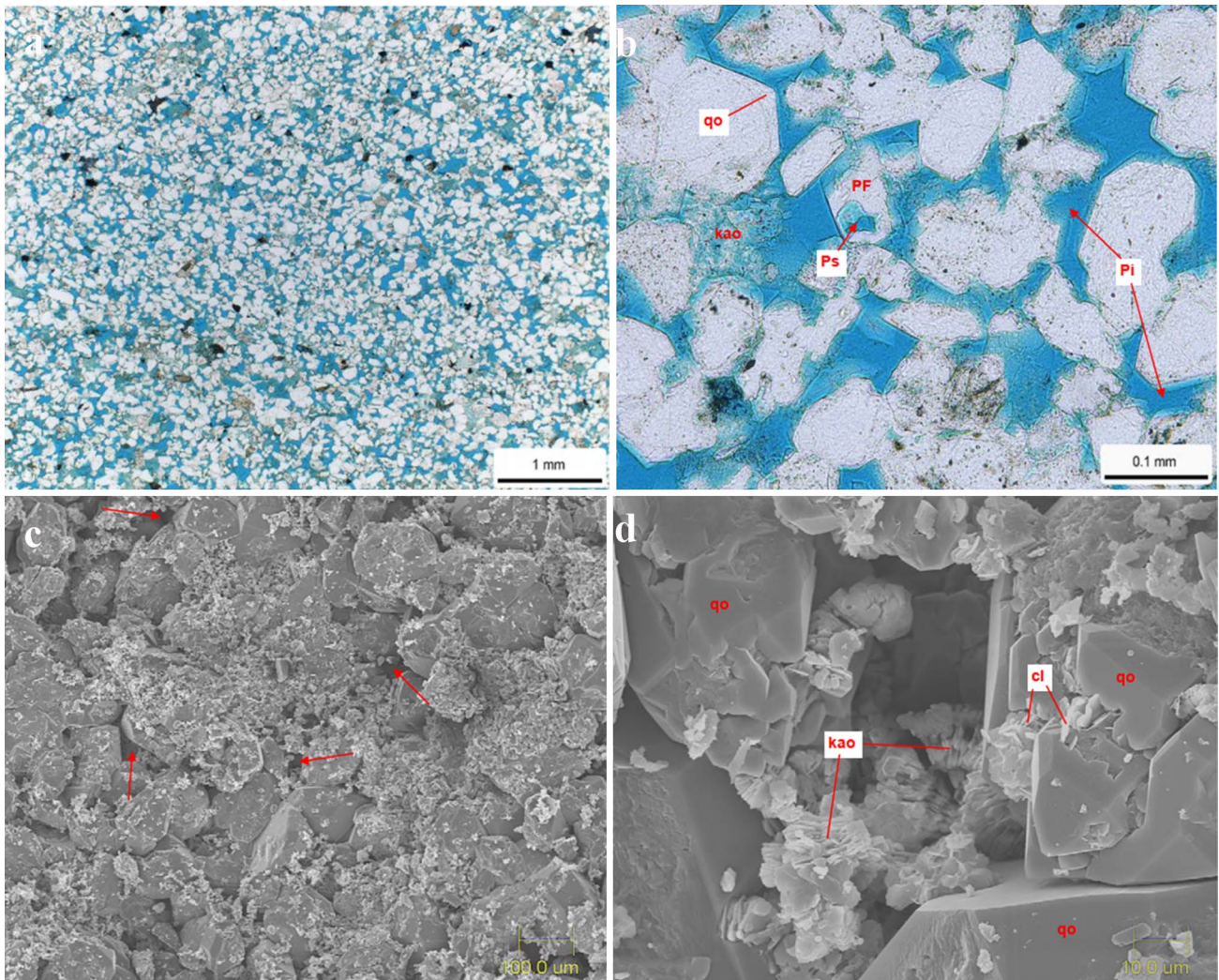


Fig. 12 **a, b** Photomicrograph of fine-grained sandstone sample at 1 mm and 0.1 mm, respectively; **c, d** SEM photomicrography at 100 μm and 10 μm , respectively

Table 5 Linear discriminate function analysis to interpret variation in energy and fluidity factors using the moment method

Facies	Z_1	Env	Z_2	Env	Z_3	Env	Z_4	Env
Cgl	15.25	B	263.55	SM	-21.26	F	51.49	T
Sb	15.51	B	268.06	SM	-20.28	F	54.62	T
Sc	14.94	B	245.32	SM	-18.73	F	47.39	T
Sd	13.61	B	230.14	SM	-17.02	F	43.14	T
Sf	14.47	B	274.47	SM	-20.07	F	56.45	T
Sm	17.87	B	239.49	SM	-15.91	F	50.91	T
Sp	15.48	B	258.49	SM	-19.73	F	45.20	T
Ss	14.21	B	249.50	SM	-19.10	F	43.50	T
Sxr	26.43	B	290.76	SM	-16.00	F	72.71	T

Facies B1 units are composed of amalgamated sandstone layers in which grading and well-defined sedimentation units may be absent to poorly developed, but most consist of stacked graded sedimentation units (Fig. 18a).

Water-escape structures, especially dish structures form with this unit and are isolated vertical water-escape conduits with sets of subvertical water-escape sheets (Fig. 18a). These are similar to the S3 divisions of Lowe

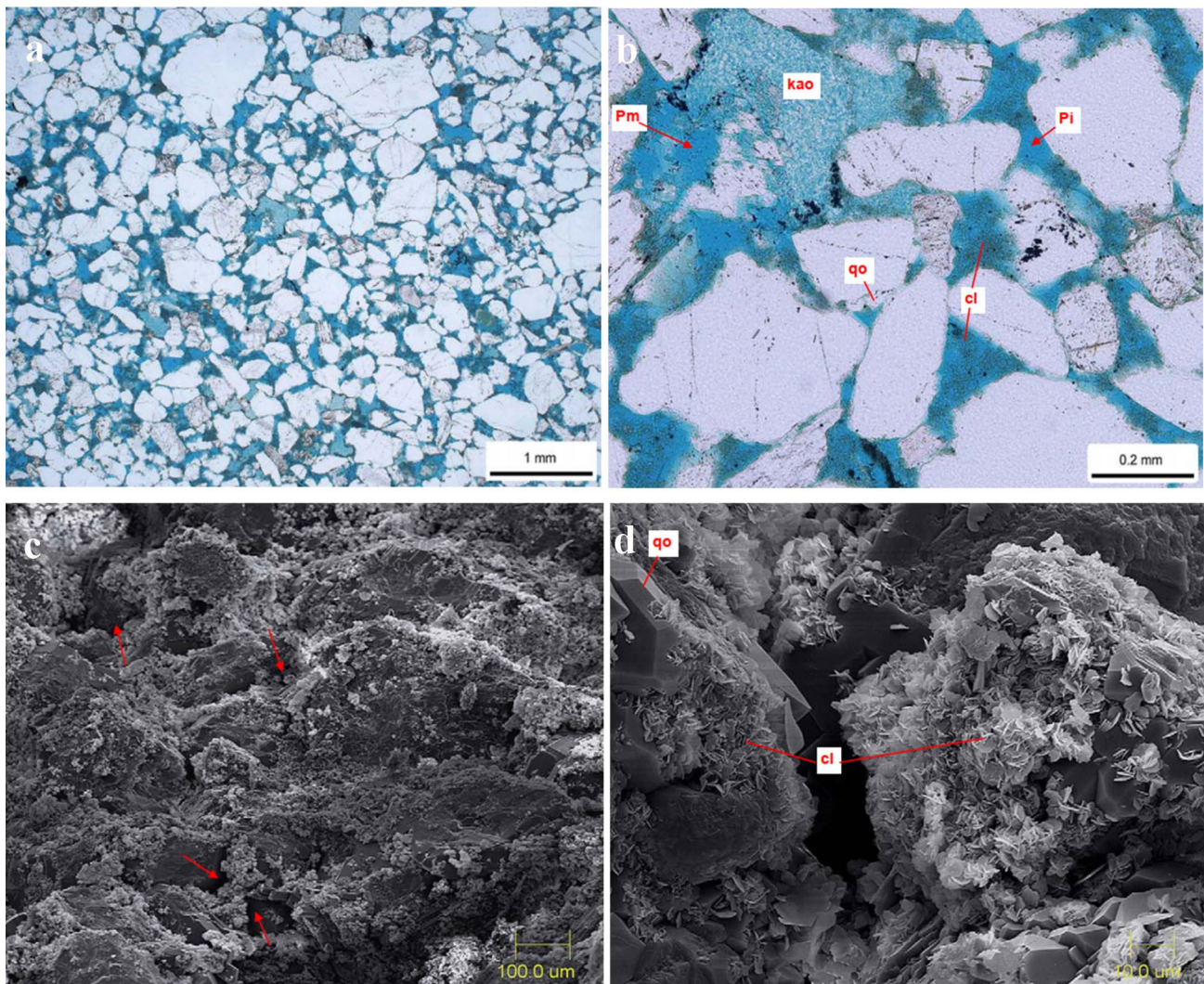


Fig. 13 **a, b** Photomicrograph of planar stratified sandstone sample at 1 mm and 0.2 mm, respectively; **c, d** SEM photomicrography at 100 μm and 10 μm , respectively

(1982) deposited by collapsing high-density turbidity currents.

Facies B2 unit comprises of many thick-bedded sedimentation units in the MH1 reservoir unit. They are composed of stacked, graded turbidites up to 150 cm thick made up largely of Bouma Tb divisions (Bouma 1962), which are deposited as a result of bed load sedimentation under high-velocity plane-bed conditions (Fig. 18b). These Tb divisions show alternating light quartzo-feldspathic laminations and dark laminations rich in mud grains and carbonaceous matter. They are in some instances underlain by thin massive Ta divisions and in most beds are overlain by thin T_{de} divisions (Fig. 18b). These beds were deposited by direct suspension sedimentation (Ta) and low-density turbidity currents (T_c, T_d, T_e) but the flows may have been exceptionally thick and/or long-lived.

The medium-bedded sandstone and mudstone lithofacies are composed of 20–80% sandstone beds, the majority of which are 10–50 cm thick with sections of thin-bedded sandstone and mudstone (Fig. 19). Bouma T_{abc} divisions or combinations of these divisions are included in these beds (Fig. 19a, b). The bases are less erosive than those of sand beds in thick-bedded lithofacies, reflected in the common preservation of mud units representing T_{de} divisions between the sand beds (Fig. 19). These beds were deposited as a result of declining, late-stage high-density turbidity currents and successor energetic low-density turbidity currents.

Facies B4 is made up of more than 80% sandstone, which forms thin, very fine-to-medium-grained turbidites up to 10 cm thick (Fig. 20). Bouma T_b and T_c divisions dominate the thin sandy turbidites, which are separated by thin muddy laminations, most of which are 1 mm thick (Fig. 20a, b and

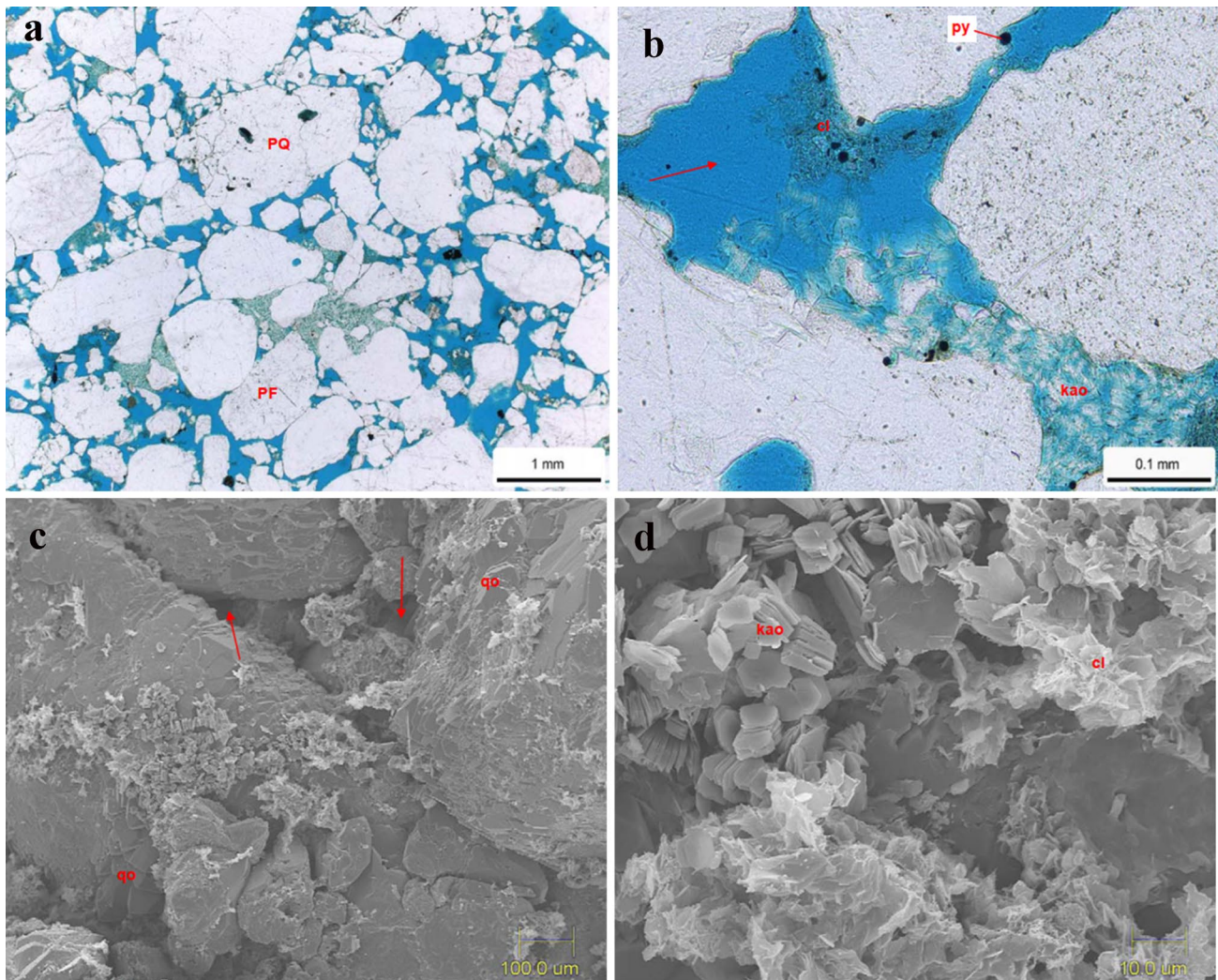


Fig. 14 **a, b** Photomicrograph of structureless sandstone sample at 1 mm and 0.1 mm, respectively; **c, d** SEM photomicrography at 100 μm and 10 μm , respectively

c). Low-density turbidity currents deposited these beds, but the sparse development of capping T_{de} mudstone or post-flow hemipelagic mudstone divisions is unusual in the cores (Fig. 20). These low-density turbidites may be devoid of mud, or the majority of silt. In addition, the likelihood of mud bypassing and depositing farther downslope may be likely. The lithofacies of thin-bedded sandstone and mudstone are well-developed in the WI (Fig. 7a). These are the dominant lithofacies in the out-of-channel levee and more distal splay deposits in most deep-water sequences.

Facies C: Mudstone

The mudstone lithofacies is made up of mudstone that contains 10–20% sandstone beds, the majority of which are fine-grained and less than 10 cm thick (Fig. 21). The deposition was generally accomplished through (1) Very low energy,

mud-rich turbidity currents and, in some cases, hemipelagic sedimentation and (2) As a result of Mass transport deposits.

Most of the mudstone in the Upper Mahogany interval is turbiditic mudstone, representing the deposits of low-density, very low-energy turbidity currents (Fig. 21a, b). The deposition was generally by very low energy, mud-rich turbidity currents. In the cored mudstone section representing MH3 and in much of MH1 (Fig. 21c), mudstone is mainly fissile mudstone with few or no associated turbidites (Fig. 21). This mudstone may represent hemipelagic sedimentation with burrowing ranges from absent to intense.

Many mass transport units are largely composed of mudstone, and many of these mudstone units exhibit evidence of local mixing and recumbent folding. The majority of the mudstones appear to have been deposited as very loose, low-strength bottom sediments that were subject to widespread failure and downslope movement (Fig. 21a, b and c).

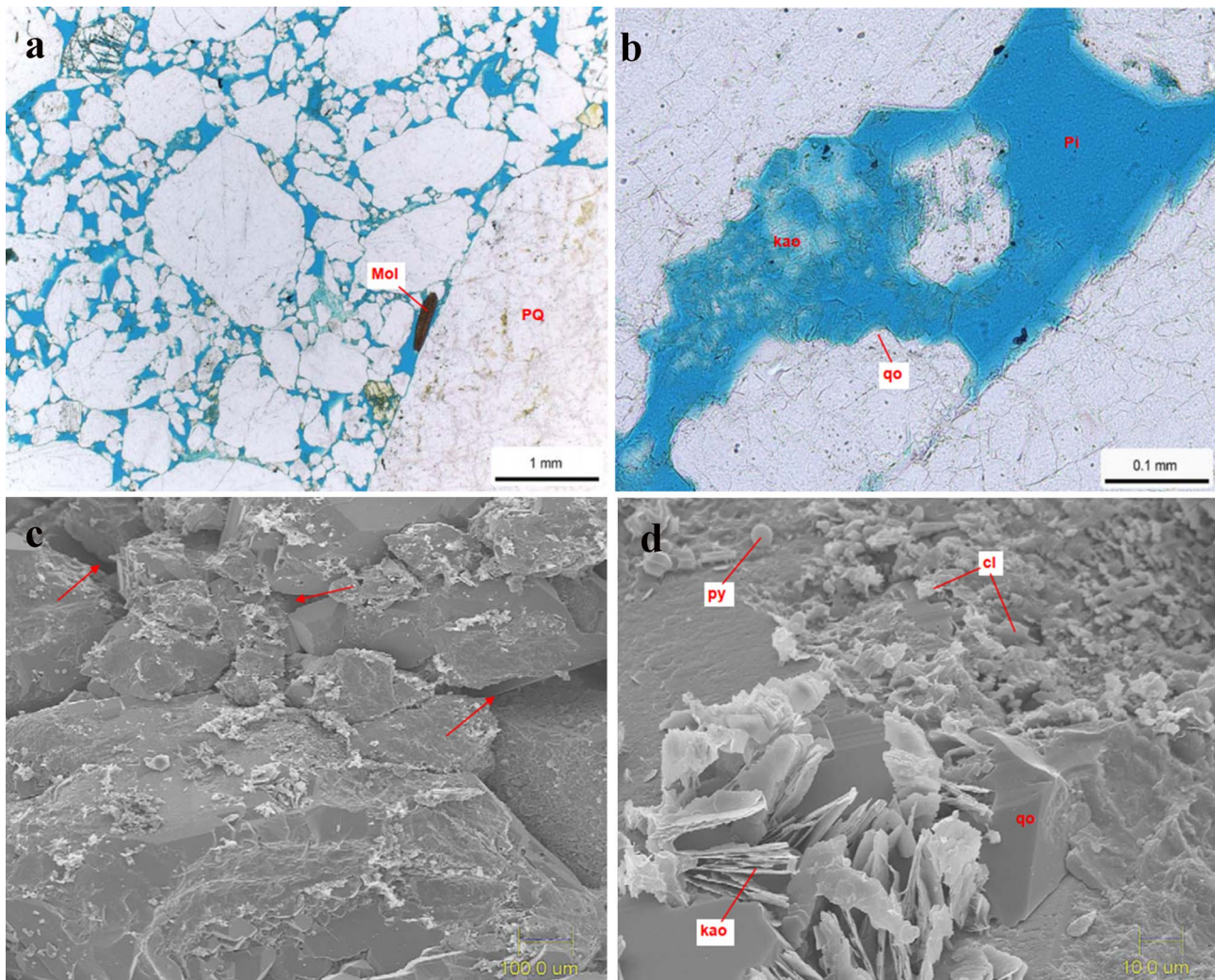


Fig. 15 **a, b** Photomicrography of conglomerate sample at 1 mm and 0.1 mm, respectively; **c, d** SEM photomicrography at 100 µm and 10 µm, respectively

In addition, units representing debris flows, slides and slide blocks, and slumps are among them. These are primarily muddy units, owing to the abundance of mud on the seafloor and the presence of significant local slopes (Fig. 22a). Many are transitional into mudstone sections and are made up of mudstone chunks and blocks in a homogenized mud matrix. In other sections, more heterogeneous sections failed and the mass transport units are mixtures of mudstone clasts and thin-bedded mudstone and sandstone clasts and blocks in a matrix of sandy mudstone (Fig. 22b, c and d). It was difficult to determine whether mudstone units associated with mass transport deposits were intact mudstone layers or mudstone blocks within the mass transport complexes in some cases. Slide or displaced blocks have tilted stratification, internal disruption, common micro faulting of internal laminations (Fig. 22b), and/or shearing along with their contacts with adjacent units (Fig. 22c).

Reservoir quality

In terms of reservoir quality sandstone, logarithmic cross-plots of porosity vs. permeability derived from data sets of each sandstone facies for all wells (W1, W2 and W3) were analyzed (Fig. 24). The logarithmic cross-plot, which is colour coded by facies type, does not precisely separate the sandstone facies, but it does indicate reservoir quality (Fig. 24). Based on these values, a high quality (> 10% porosity, > 10 mD permeability), moderate quality (> 10% porosity, 10 mD permeability), and low quality (porosity 5% and permeability 0.01 mD) reservoir sandstone facies class were identified. A significant number of data points are less than 10% porosity and 10 mD permeability. These are typically well-cemented layers with pervasive calcite cement that has occluded microporosity (Figs. 11c, 12c, 13c, 14c, 15c and 16c).

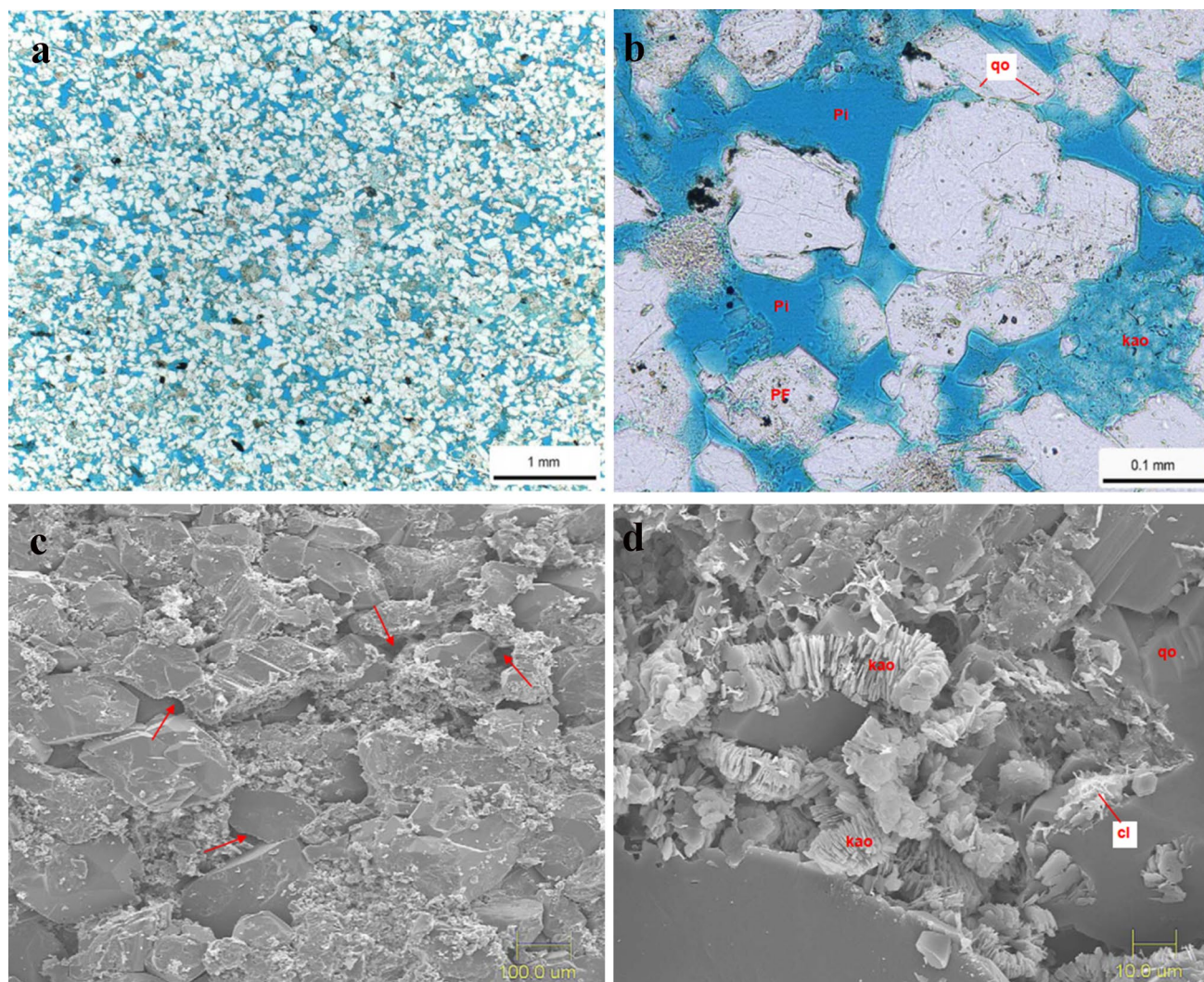


Fig. 16 **a, b** Photomicrography of ripple-cross laminated sandstone sample at 1 mm and 0.2 mm, respectively; **c, d** SEM photomicrography at 100 μm and 10 μm , respectively

The low-quality sandstone represents sandstone samples that have been extensively cemented by calcite, resulting in occluded porosity and reduced reservoir potential (Figs. 11, 12, 13 and 15). This sandstone contains bioclasts, and the calcite may have been mined locally (Fig. 23). This is a diagenetic reservoir quality control as indicated in Figs. 10c, 11c, 12c, 13c, 14c, 15c, and 16c.

A grey filling (Fig. 24) delineates moderate reservoir quality samples. These are primarily argillaceous sandstone (Sa), bioturbated sandstone (Sb), fine-grained sandstone (Sf), and weakly stratified sandstone (Sm). Reservoir quality is likely to be poor in these lithofacies. The porosity measured in these samples is most likely microporosity.

Pebbly (Sc), planar laminated (Sp), structureless (Ss), dewatered/deformed sandstone (Sd), and conglomerates (Cgl) appear to dominate the high-quality reservoir sandstones partitioning (black circle, Fig. 24). Sc, Ss, Sp, and Cgl samples have higher permeability values than bioturbated sandstone (Sb) and ripple cross-laminated sandstone (Sxr) types for any given porosity value (from about 10% to about 25%, as shown in Fig. 24). The majority of the sandstone samples have good reservoir quality, and many of them have permeabilities greater than 100 mD (Fig. 24). These findings suggest that reservoir quality is primarily governed by lithofacies type, with diagenetic controls also playing a vital role. Due to the thin and rare nature of these lithofacies, no core analysis data exists in siltstone (Stn) core lithofacies.

Table 6 Core lithofacies scheme for the Wells

Facies code	Lithology and texture	Dominated physical sedimentary structures	Interpretation
Sa	Argillaceous sandstones: fine shale intercalated with sandstone resulting in an argillaceous appearance. Sandstone beds are 4–10 cm thick with alternating thin mud. The colour is greyish brown	Intercalation of wispy shale and sandstone lamination	Sa sandstone was most likely deposited by gravity-driven flow caused by turbulent flow action. This may occasionally reflect the longitudinal flow progression of the turbidity current, in which the clay/silt ratio to sand increases as run-out length increases
Sb	Burrowed sandstones: medium to fine-grained and generally well-sorted sandstones. Bed thickness is typically 10–30 cm, locally amalgamated into thicker beds. Beds may display flat bases and bioturbated tops. Burrows are variable. Mud-filled sub-vertical traces occur along the top of the sandstone beds; probably <i>Arenicolites</i> . Large, inclined, sand-filled burrows are evident and are identified as <i>Thalassinoides</i> . Colour ranges from dark yellowish-brown to yellowish-grey	NN	The sandy substrate colonized by diverse range of burrowing organisms. Sand-filled burrows may indicate sand-rich bypassing flows. Flows supplied oxygen and nutrients to the colony of suspension-feeding crustaceans that formed the burrows
Sc	Pebbly/granular sandstone: moderately to poor sorting, medium to very coarse grain with some clay clasts and reddish clasts. Beds are generally greater than 20 cm and up to 1 m thick. The colour is variable from greyish to dark yellowish-brown	Weak planar stratification	The sandstone, Sc was transported and deposited by concentrated high energy turbidity current and deposited probably by frictional freezing
Sd	Dewatered/deformed sandstone: medium-to-coarse-grained, moderately well-sorted sandstone. Bed thickness is generally greater than 30 cm. Colour is greyish brown	Dewatered structures, e.g., pipes and mottles and dish structures	Sd was deposited by collapsing turbidity flows which results in rapid deposition of sediment. This rapid process results in the formation of dewatering structures and when acted upon by gravity along unstable slopes, slump folding and deformation occur
Sf	Fine-grained sandstone: fine-grained and well-sorted sandstone with argillaceous laminations. Bed thickness is approximately 10 cm. The colour is generally medium to light grey	Wavy, parallel to non-parallel lamination. The lamination is made up of interbedded heteroliths	The sediments are well-sorted and generally well structured. Sediment deposition may be attributed to a low current environment
Sm	Weakly stratified sandstone: greyish brown medium to coarse-grained and moderately to poorly sorted sandstone	Weak discontinuous planar to low angle cross-stratification	Sediment transportation by a high energy turbidity current. The weak structures may be as a result of rapid deposition by frictional freezing
Sp	Planar-stratified sandstone: greyish brown-to-yellowish-grey medium to coarse-grained and moderately to well-sorted sandstone. Bed thickness averages > 30 cm	Planar stratification	These sandstones were probably deposited by the upper flow regime producing planar bedding by grain alignments
Ss	Structureless sandstone: medium-to-coarse-grained, moderately sorted sandstone. Bed thickness average greater than 30 cm. Colour is brownish grey to dusky brown. The sandstone occurs within overall graded units	Structureless or very weak structures	The sandstones may have been transported by a highly concentrated high-energy turbidity current. The lack of structures may signify a rapid frictional freezing deposition
Sx	Cross-stratified sandstones: medium-to-coarse-grained and moderately to poorly sorted sandstone. Beds thickness is generally 10–30 cm. Colour is light to dark yellowish-brown	Cross stratification	The cross-stratification is produced by migrating bedforms. The bedforms may be of a linear crested to undulate crested morphology producing planar to asymptotic cross-stratified beds. Sediment bypass may be indicated by cross-stratification

Table 6 (continued)

Facies code	Lithology and texture	Dominated physical sedimentary structures	Interpretation
Sxr	Ripple cross-laminated sandstone: fine-to-medium-grained, well-sorted sandstone with homogeneous grain size within individual beds. Beds average approximately 40 cm thick. The colour is dark yellowish-brown	Ripple cross-lamination and well-defined planar lamination	The cross lamination is produced by migrating current ripples. Sediment bypass may be indicated by cross-stratification
Stn	Siltstone: it is uncommon. Silty sediment is in thin beds 10 cm thick. One layer may not be in place and may consist of a large deformed cobble clast	Lamination	Distal low-density turbidite deposits may be represented by bedded siltstones. Several sheets might very well consist of large cobbles that have been eroded when semi consolidated
Cgl	Conglomerate: clast supported sediment with granule to pebble grade detrital quartz grains. Beds averages within 10 cm to 30 cm. Colour is medium grey to greyish brown	NN	Extremely coarse material is transported by energetic bedload processes. May indicate channel bases or bypass zones
Ds	Sand-dominated debrite: deformed mud clasts suspended in a sandy matrix. Mudclasts are pebble to cobble grade. Clasts are folded and highly angular, display internal lamination and were probably semi consolidated when eroded. Clasts are suspended in a medium-to-coarse-grained sandy matrix. Bed thickness averages > 30 cm. Colour is generally medium grey to greyish brown	Lamination	The large size and deformed nature of the mudstone clasts indicate that they were not transported far from their source area (local) and were probably partially indurated before erosion
Hp	Planar-laminated heteroliths: Approximately 25:75 sandstone and mudstone heteroliths. The sandy lamination thickness averages approximately 3 cm. The colour is dark grey to light grey	Planar lamination	The mudstone portion was probably deposited by suspension fallout. The interlaminated fine silty and sandy material may represent very distal turbidite laminae
Hi	Irregularly laminated heteroliths: Approximately 25:75 sandstone and mudstone heteroliths. Sandy laminae are very fine-grained and well-sorted. Lamination is on a cm scale and is generally irregular. The colour is brownish-grey to black	Lamination	The mudstone portion was probably deposited by suspension fall out from distal turbidite flow. The interlaminated fine silty and sandy material may represent very distal turbidite laminae formed along an unstable slope
Hs	Sandy heteroliths: Approximately 50:50 to 75:25 sandstone mudstone heteroliths. Sandstones are fine to very fine-grained and well-sorted. The colour is light grey to greyish yellow	Lamination	The sandy mud laminated heteroliths material may represent very proximal turbidite laminae formed along an unstable slope
Hb	Bioturbated heteroliths: Approximately 50:50 to 75:25 sandstone mudstone heteroliths. Sand laminae are very fine-grained and well-sorted. Bioturbation is extensive with evidence of horizontal sand-filled, mud-filled burrows	Lamination	Colonization of sediment surfaces by a diverse range and abundant volumes of burrowing organisms. Oxygenated setting
I	Injectite: sandstone injected into mudstone or heteroliths. Disrupted margins and internal deformation are evident. Mainly as dykes with irregular margins and upward tapering profile	NN	Mobilisation of overpressured sands by liquefaction processes during (hydro) fracturing

N/A not noticed

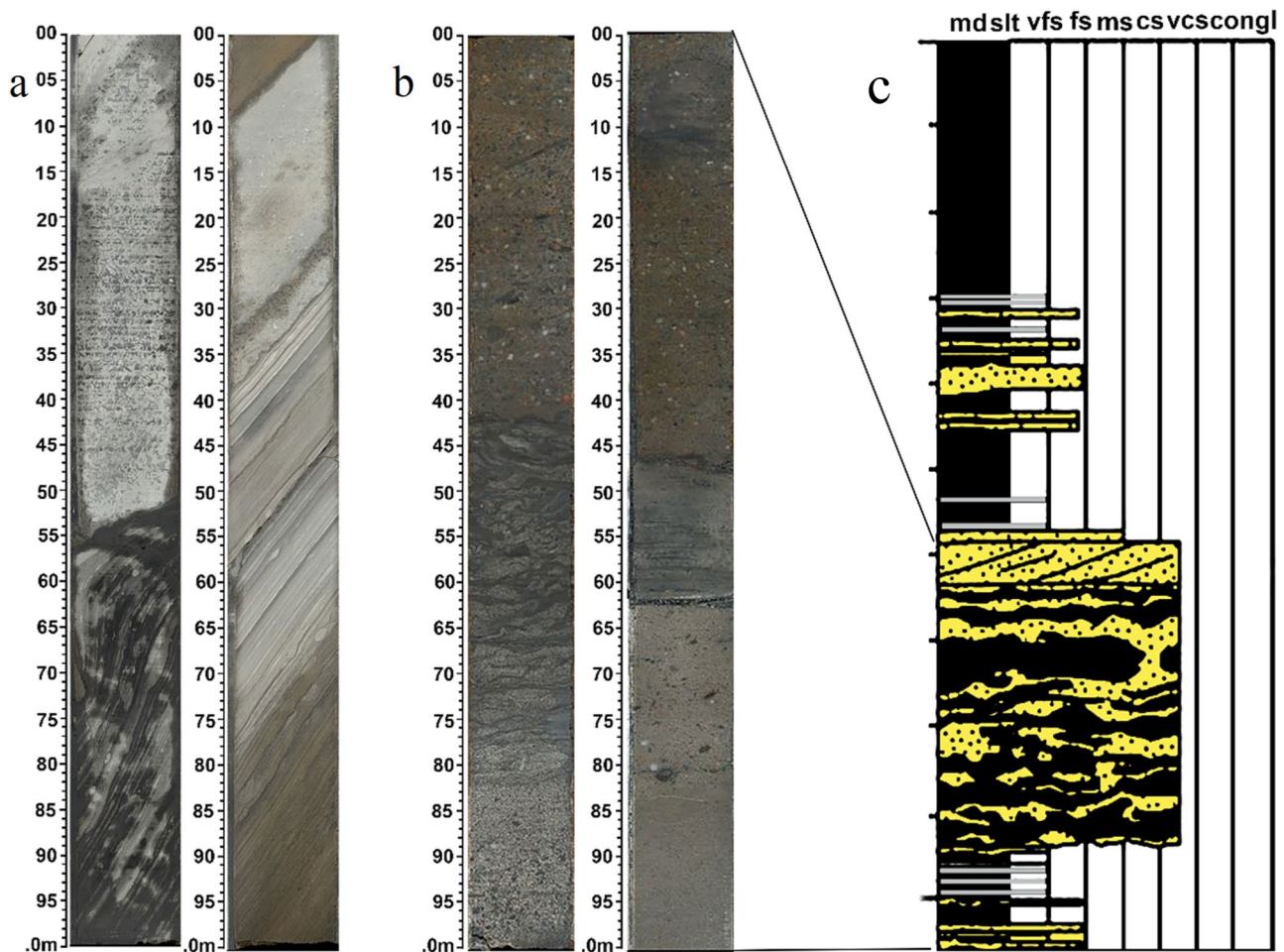


Fig. 17 Conglomerate lithofacies. **a** Extrabasinal-clast conglomerate occurring as a single layer and a mud-cast conglomerate observed at 4037–4037.28 m and 4046.8–4047.75 m, respectively, in W1, **b**

thin units of mud-clast conglomerate form numerous beds observed (3201–3202 m) in W3. **c** Sedimentological log of the conglomerate facies for W1

Discussion

Depositional model of the Turonian Reservoir

The 3D seismic volume (Fig. 3), Sum of negative Amplitude (SNA) maps (Figs. 25 and 26), and cores from wells W1, W2 and W3 documents the evolution of the MH1 and MH4 reservoir system. In general, two main evolutionary stages can be identified: (1) pre-channel events, and (2) formation and evolution of channel complex.

MH1/MH4 Pre-channel event

The lowest symmetric cycle at the base of MH1/MH4 in core is too small to be resolved unambiguously using seismic data (Figs. 25a and 26a). In the pre-channel event, the site of the channel complex was primarily covered by mudstone containing thin sandstone interbeds representing fine-grained muddy turbidites that have widely suffered post-depositional

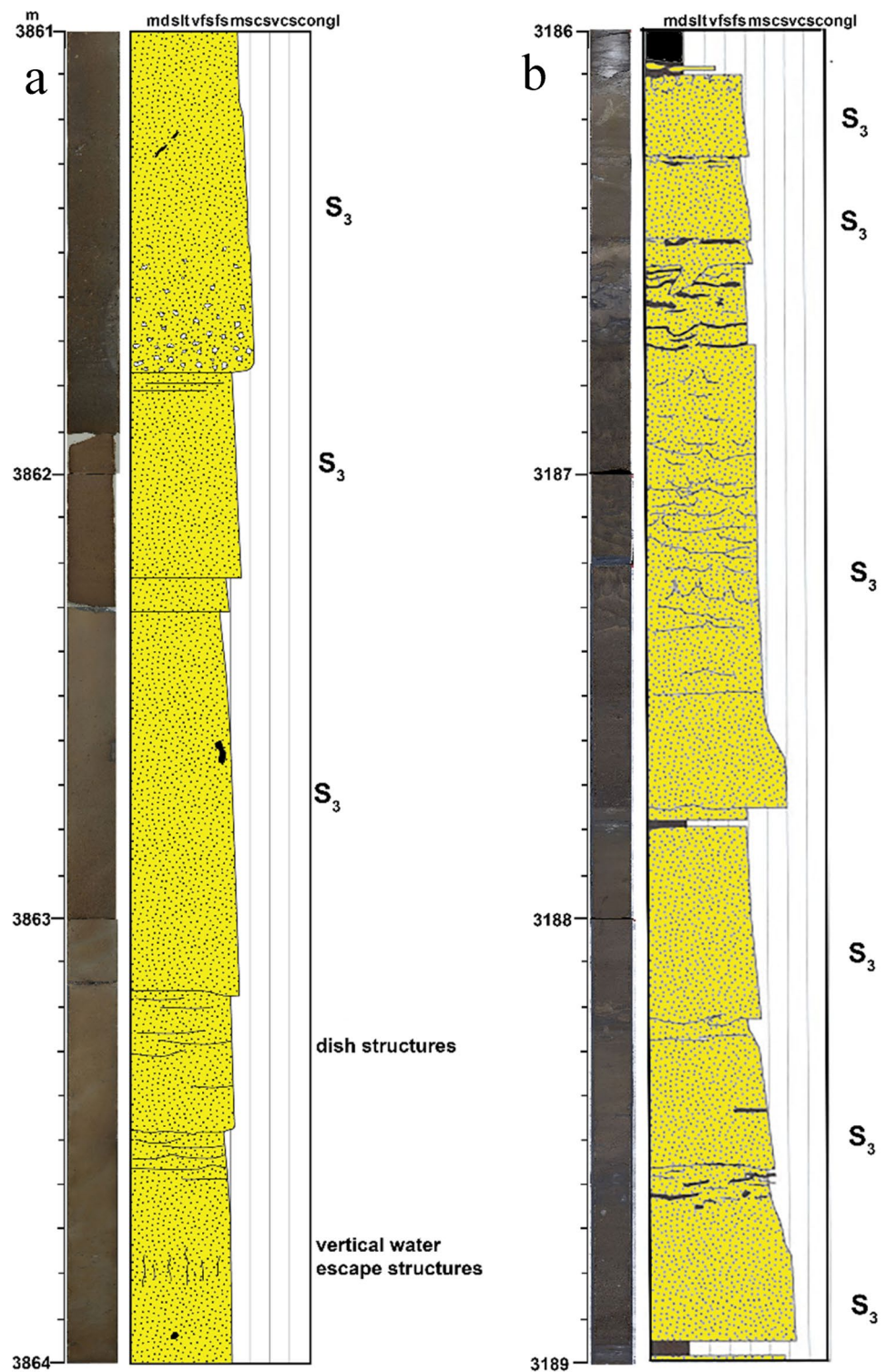
movement and flowage to form mass transport deposits (Figs. 25a, 21a, c).

Formation and evolution of the MH1/MH4 channel complex

MH1 channel complex The Lower Mahogany interval is characterized by cored intervals from wells W1, W2, and W3 representing the lower fan channel complex (Fig. 25). The development and evolution of the MH1 channel complexes are discussed below.

Development of the MH1 channel: SNA maps show that the channel complex was initiated by overbanking, crevasse development, and splay formation along the northern to the southeastern section of the Jubilee unit (Fig. 25). Flows moving down the eastern side of the sediment source diverted through an erosive breach and spilt westward into the Mahogany area (Fig. 25a). However, the existence of a small linear area of sand deposition inside the channel in this area before crevasse formation (Fig. 25a, b) suggests

Fig. 18 Thick-bedded, massive to dish-structured sandstones were observed in **a** W1 and **b** W3. The structural framework depicts deposit of the S3 divisions (Lowe 1982) by direct suspension sedimentation from high turbidity current. S3 divisions are formed as a result of a further fallout of suspended-load leading to sediments deposition directly through suspension sedimentation



that it was a low spot along the levee. The uppermost parts of the large flows moving eastward, prior to crevasse erosion, may have topped the levee at this point (Fig. 25b). Sand thickness distribution (Fig. 27a) and flow patterns from the SNA maps (Fig. 25a, b) suggest that just up-system from the point of breakthrough on the northern bank, the flows

moving westward went around a tight bend on the central side of the channel that would have diverted them to the southwest across the channel (Fig. 25c). The western and southern branches of the initial off-channel development were incorporated into the main MH1 reservoir development system as overbank splays that fed off the developing

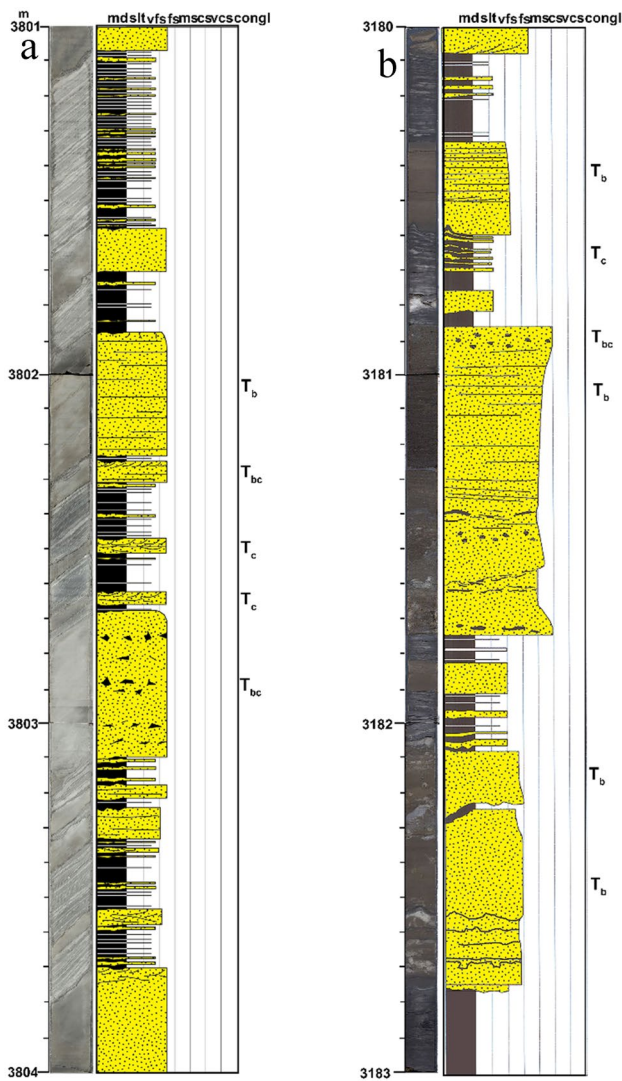


Fig. 19 Medium-bedded sandstone intercalation with mudstone. Most involve various combination of the Bouma divisions: T_a , formed by direct suspension sedimentation; T_b , deposited by bed load sedimentation under high-velocity plane-bed conditions; T_c , deposited as bed load under low-velocity conditions with a rippled bed; T_d , deposited under very low-velocity condition; and T_e , silt and mud deposited after the flow has ceased. **a** Thick sandstone beds with cross lamination Bouma T_c division at the tops of beds and flat laminations T_b division occurring in W1. **b** Thick sandstone beds with cross lamination Bouma T_c division at the tops of beds and flat laminations T_b division occurring in W2

channel course at meander bends (dark blue of the frontal splay and the gold for the crevasse splay in Fig. 25c). The well-defined meandering channel coincides well with the route and specific meanders that characterized the MH1 channel (Fig. 25c). Flows coming out of this mender bend were aimed directly toward the point of breakthrough along the central levee (Fig. 28). This configuration would have enhanced the levee erosion and overbanking of the flows at this point (Figs. 25c and 28).

In addition, overbanking was preceded by the deposition of about 10 m of sandy strata (4050–4060.3 m) that includes a middle section of 5 m thick of thin-bedded sandstone (4053.15–4058.3 m), overlain and underlain by thin-bedded sandstone and mudstone (Fig. 23a). There is a single thick sandstone bed from 4055.0 to 4055.75 toward the middle of the cycle (Fig. 23a). This symmetric cycle lacks evidence for channels and erosion and represents deposition from strictly low-energy, low-density turbidity currents. It is interpreted to represent the downslope part of a small lobe or splay (Fig. 25b, c). The deposition of sediment within the channel may have been sufficient to trigger more extensive overbanking along the channel levee, erosion, and eventually, avulsion, as inferred from other systems (Kolla 2007; Lowe 2019; Stow and Smillie 2020). The earliest major overbanking and crevasse splay development along the main course of the channel complex (Fig. 25c) show the development of a small splay with southern and central lobes (gold polyline in Fig. 25c). Some sandy flows were diverted into a distal southern lobe running along the southern edge of the main channel levee (Fig. 25c). This distal lobe may be the distal tip of a larger sand body that is present at the base of the LM2/MH1 interval to the south (Fig. 25c), or it may represent a separate small lobe developed north of the main sand fairway during lower LM2/MH1 sedimentation.

As this splay developed, the locations and geometries of channels and lobes shifted across the depositional surface (Fig. 25b, c). Eventually, the outlines of the channel took shape, with enlargement of the middle part of the avulsion splay from the main channel flowing eastward (Fig. 25). However, the main channel itself was not yet well-defined toward the southeastern section. At this time, there was also localization of silt and mud deposition in more downslope areas into narrow splay-like features, similar to the description by Lowe et al. (2019).

The upper section of the core log (Fig. 23a) indicates two overall trends: (1) symmetrical pattern composed of upper and lower sections of medium-bedded sandstone and mudstone and a central core of thick-bedded sandstone meaning that the lowest and uppermost 4 to 5 m are made up of sandstone beds that are distinctly thinner and finer than those comprising the middle part of the cycle. (2) The lowest 5 m (4040.1–4045 m) includes a basal coarsening- and thickening-upward zone and an overlying minor symmetric cycle. All overlying small-scale internal cycles are fining-upward cycles, from 1.5 to about 3 m thick (Fig. 23a). These overall features suggest that this section represents a thick splay system (Fig. 25c). It indicates a broadly progradational at the base but the top was dominated by small channels that crossed the splay surface so that the waxing of splay activity is reflected in the coarseness of the fining-upward channel fill units (Fig. 28). Upslope this splay may show an increasing proportion of high-density flow deposits. Downslope, the

Fig. 20 Thin-bedded sandstone and mudstone intercalation. Most involve various combination of the Bouma divisions: T_{a1} , formed by direct suspension sedimentation; T_{b1} , deposited by bed load sedimentation under high-velocity plane-bed conditions; T_{c1} , deposited as bed load under low-velocity conditions with a rippled bed; T_{d1} , deposited under very low-velocity condition; and T_{e1} , silt and mud deposited after the flow has ceased. **a** Fine-grained thin-bedded turbidites deposited by low-density turbidity current showing T_{c1} , T_{d1} , and T_{e1} turbidite division for W1. **b** Fine-grained thin-bedded turbidites deposited by low-density turbidity current showing T_{c1} and T_{bc1} turbidite division for W2, and **c** thin-bedded turbidites deposited by low-density turbidity current showing T_{c1} and T_{bc1} turbidite division for W3



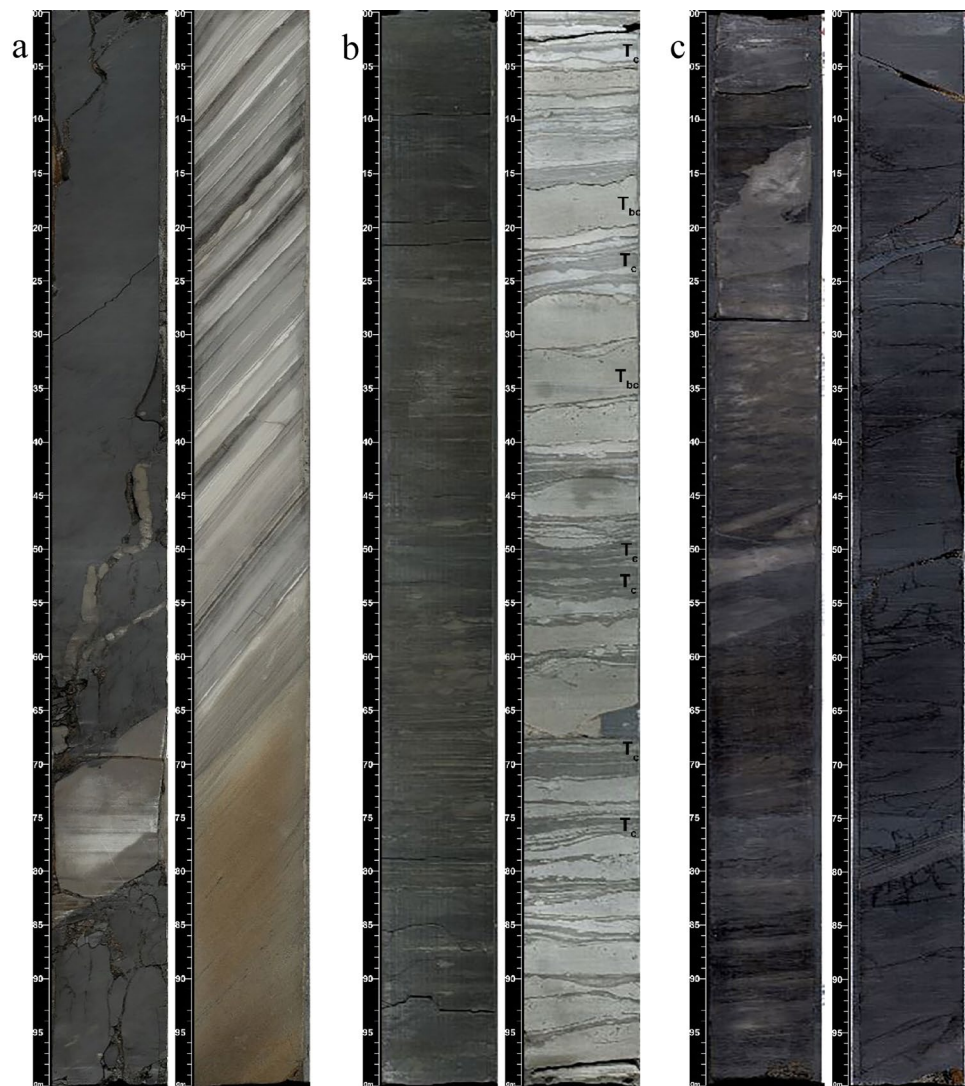
Tb-dominated thick-bedded turbidites with poorly developed Tde divisions may grade into sections of thin-bedded sandstone. These two Lower Mahogany cycles probably represent more distal similar splay systems (Fig. 28).

Overall, the Lower Mahogany LM2/MH1 sand reflects the development of a large, Southwestern-trending sand fairway south of W1 (Fig. 28). During the evolution of this fairway, a splay- or finger-like sand body developed along its northwestern margin extending to the east off the channel area (Figs. 25 and 28). This splay may have developed toward the end of a distributary formed by the upslope bifurcation of the main channel or as an overbank splay along the side of the main channel, which lay to the south (Fig. 28).

MH4 channel complex The MH4 reservoir unit shows sand accumulation as a series of three main northward off-

set stacked bodies that successively onlapped the southwestern basin margin (Fig. 29). In the W1 core, the lowest sandstone bed, 3872.6–3878.7 m, overlies a dense, black fissile mudstone marking a regional interval of fine hemipelagic sedimentation. It lacks clear trends in grain size or bed thickness. The overlying sandstone from 3857.75 to 3871.1 m forms a well-defined lobe that was characterized by the abrupt flooding of the sediment fairway by high-density turbidity currents (Fig. 26). This unit probably represents lag deposits, deposited and worked by flows that were largely bypassing and transporting most of their sediment downslope (Fig. 26b). The dominance of amalgamated S3 divisions and the immaturity of the lower part of this section suggest that well W1 was located in a proximal setting on a lobe.

Fig. 21 Mudstone lithofacies were observed in all wells **a** W1, **b** W2 and **c** W3. Most of these mudstones are characterized by thin silty or sandy interbeds and show evidence of deposition by a very fine, low-density turbidity current. Most involve various combination of the Bouma divisions: T_a , formed by direct suspension sedimentation; T_b , deposited by bed load sedimentation under high-velocity plane-bed conditions; T_c , deposited as bed load under low-velocity conditions with a rippled bed; T_d , deposited under very low-velocity condition; and T_e , silt and mud deposited after the flow has ceased



The development of these MH4 units can be interpreted in the context of the overall sedimentation in this area. The northeast–southwest-trending sand thick representing the lower MH4 sandstone unit (Fig. 27b) lies along the northwest edge but slightly north of the underlying thick sand body in MH1 (Fig. 29). At least one well-defined mud-filled in the lower MH4 channel can be seen crossing both the MH4 and the MH1 sand belts (Figs. 26a and 25a, respectively). These features suggest that during early MH4 sedimentation, a shallow topographic low existed parallel to the northeast–southwest trend of the MH1 sand belt but slightly offset to the north from the zone of maximum thickness of MH1. This shallow low was the site of lower MH4 sand accumulation (Fig. 26). It was bounded to the north by the northern basin slope and to the south by a high development along the trend of MH1 sedimentation. This high may have been accentuated by differential compaction, with the thick MH1 sands showing less overall compaction than muddier sections to the north.

Erosion associated with the late-stage, largely bypassing currents may have cut or accentuated the channel shown in Fig. 26d. This channel cuts across both the northeastern–southwestern-trending depositional area of lower MH4 sands and the MH1 sand thick near well W7. This suggests that these underlying sand units did not form a significant topographic barrier on the sea floor following the deposition of the lower MH4 sands. Although a low barrier probably existed initially for the lower MH4 sands to be deposited in this area, their deposition erased this topography and allowed turbidity currents to spill to the south across the MH4 unit. The channel shown in Fig. 26c, d may have formed at this time as the flows spill across to the southwestern section.

The MH4A sand body is overlain by a thick section of mass transport deposits (Fig. 23b, c). The top of the MH4 reservoir is marked by an interval of mass transport deposits which shows that most topographic and architectural features developed during the preceding interval of sand

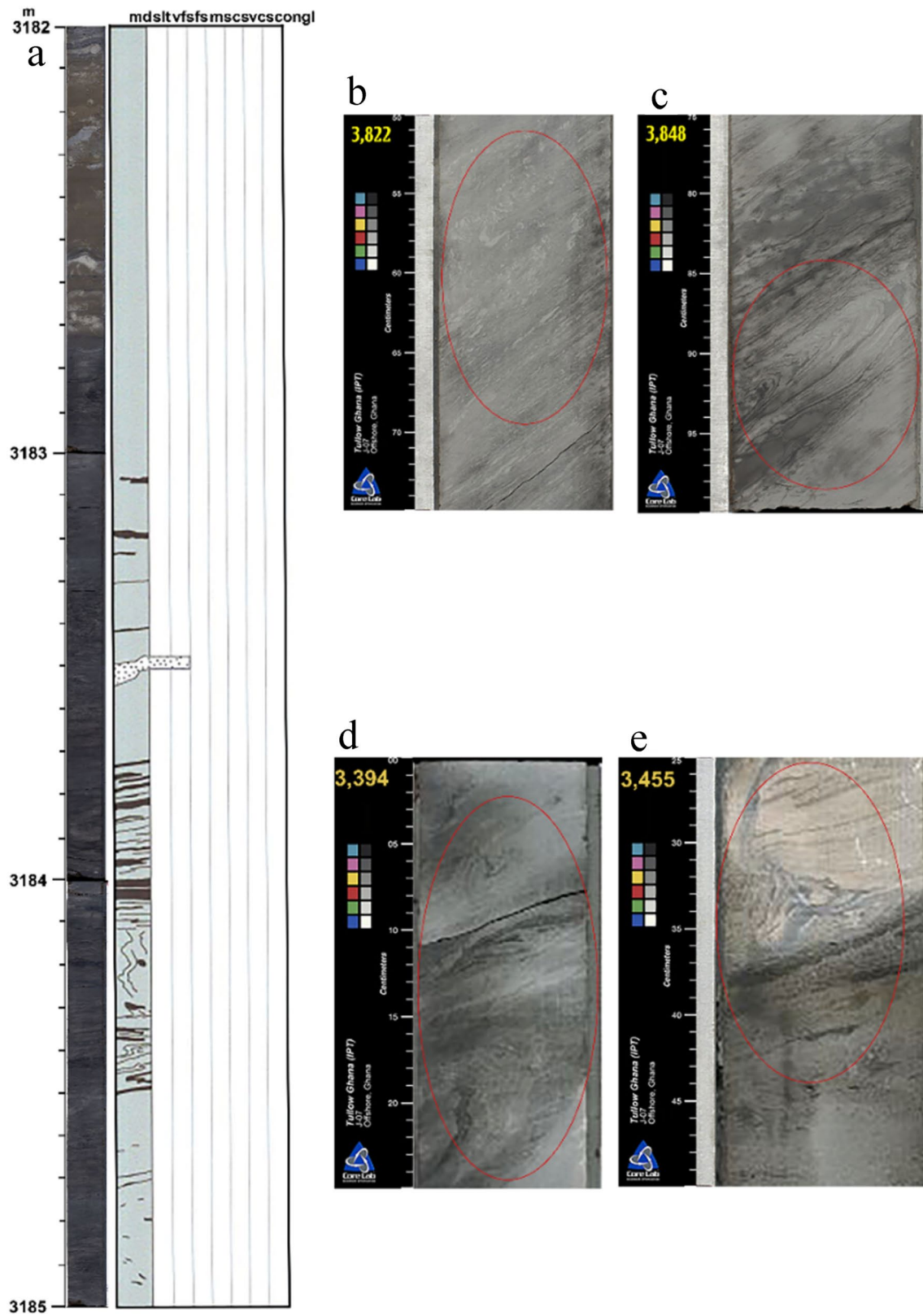


Fig. 22 Mass transport deposits observed. **a** Sedimentological log for the mass transport deposit. **b** Feature of thin sandstone beds completely disrupted and sheared within mass transport deposit observed

in W1. **c** Sheared and folded thin-bedded mudstone and sandstone observed in W1 and **d** sheared and folded thin-bedded mudstone and sandstone observed in W2 at different depths

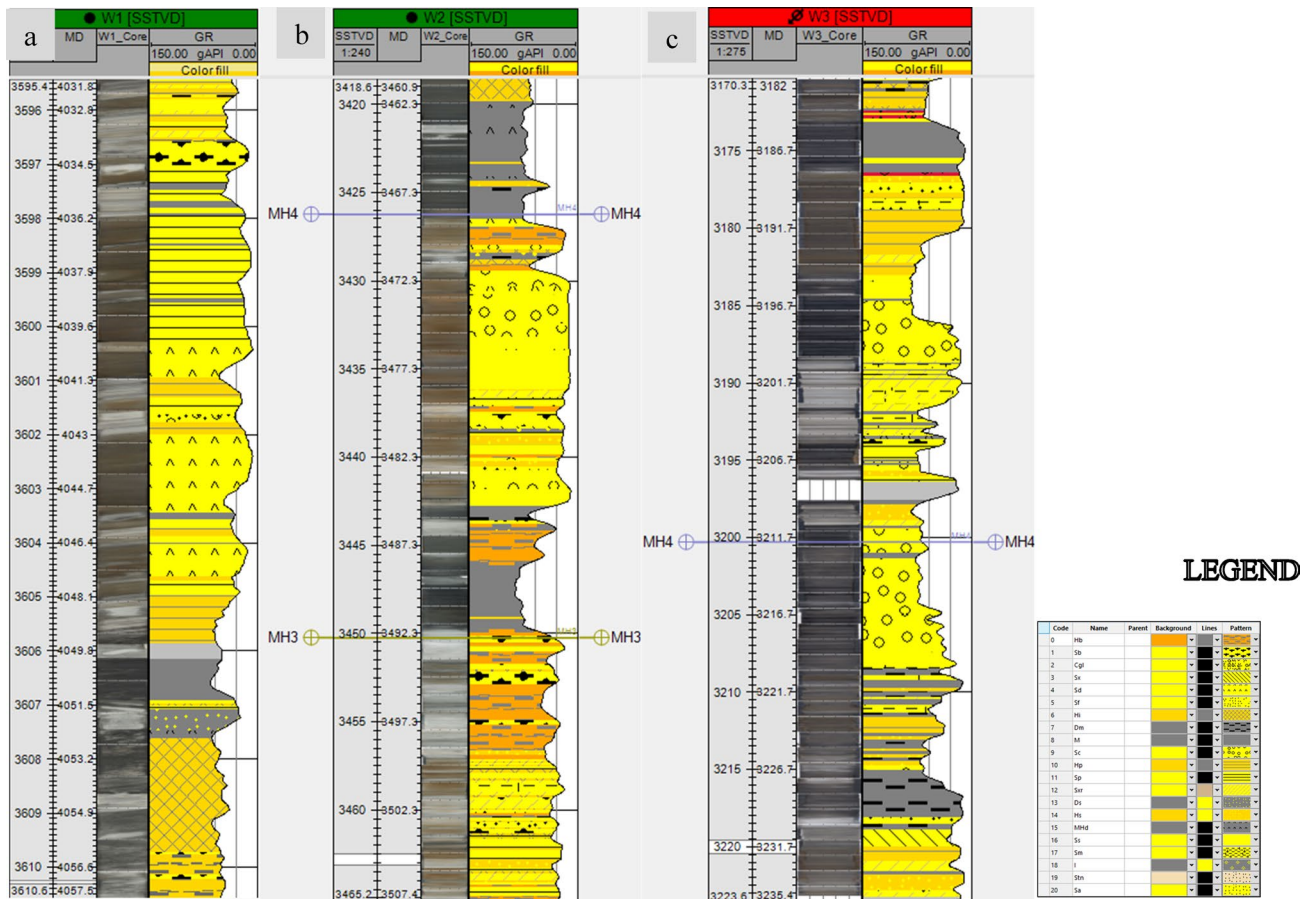
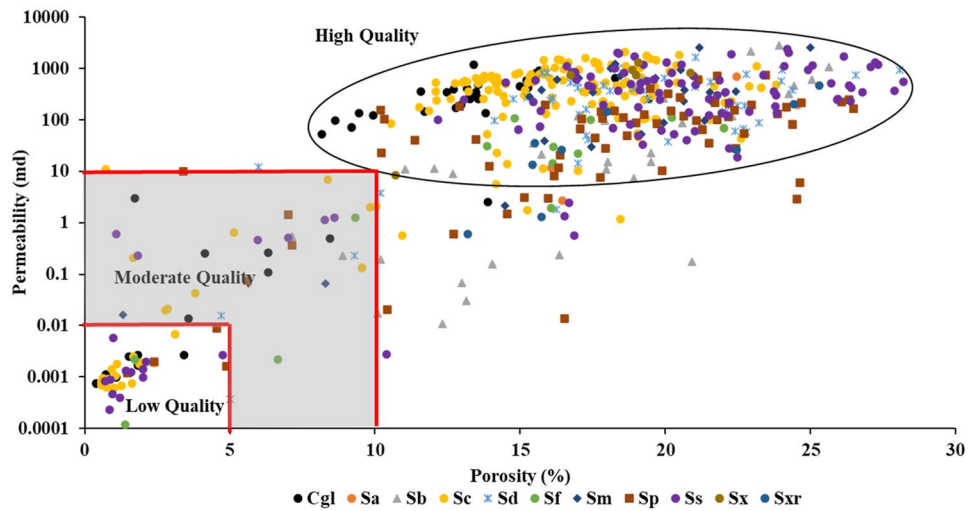


Fig. 23 Gamma ray upscaling of lithofacies to bed stack facies for well a W1, b W2 and c W3

Fig. 24 Core analysis of porosity and permeability cross plot coded by sand facies



sedimentation had been obliterated and the sediment surface was a largely featureless plain.

Sedimentation Pattern of MH1 and MH4 reservoirs

The main architectural components of this depositional setting included: (1) levee-like sections of thin-bedded mudstone and sandstone; (2) thick mass transport deposits,

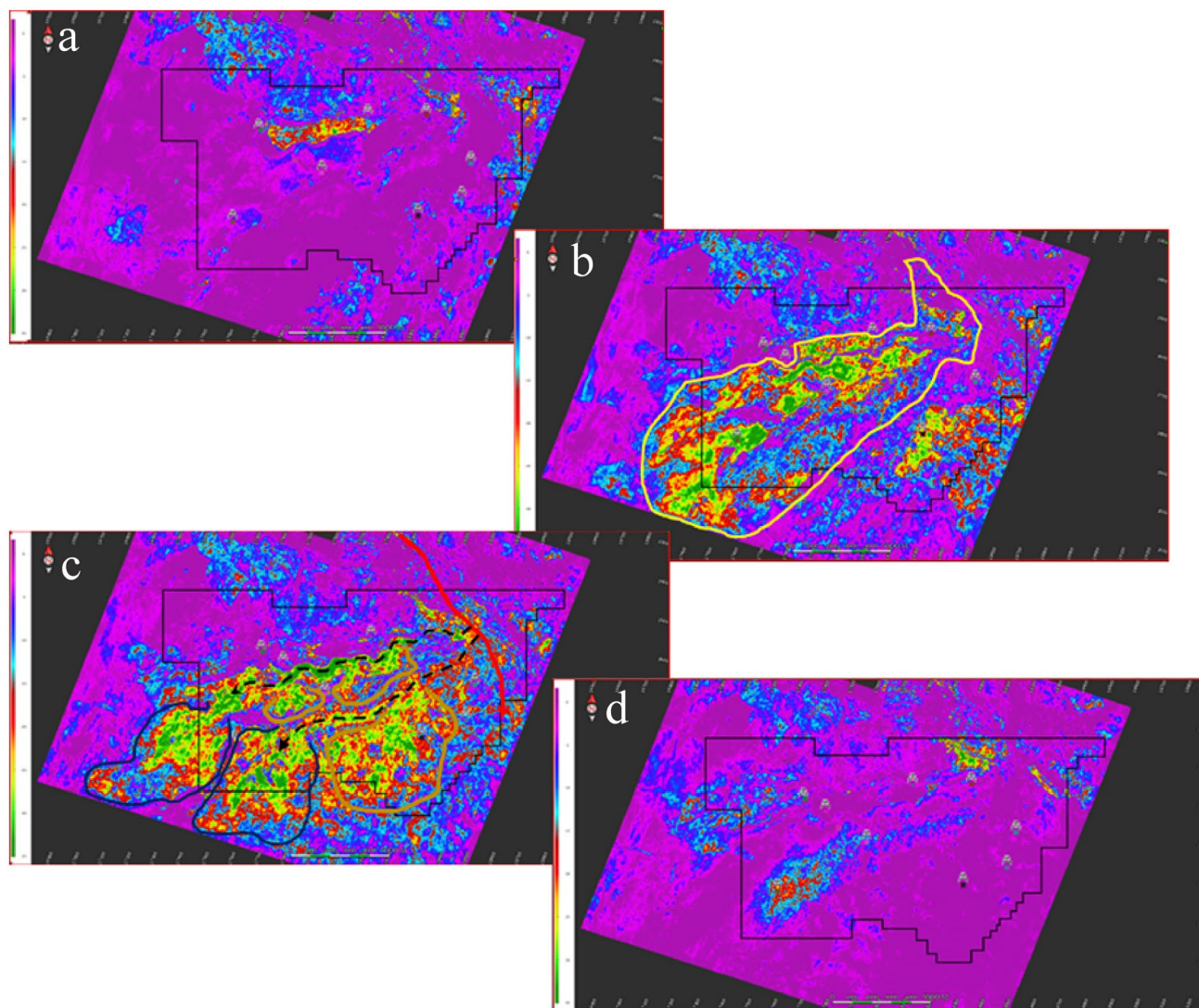


Fig. 25 Sum of negative amplitude (SNA) extraction showing the evolution of the complex turbidite system of the MH1 reservoir system. **a** Interval at the base of the MH1 unit marking an erosional surface of possible levee which is marked by abundant heteroliths and mudstones in well W1 (Fig. 21a) and mudstones in W3 (Fig. 21c). **b** Lower section of the reservoir unit representing the development of a central splay complex with the Jubilee contract area. The yellow polygon shows the channel system. **c** Interval of the MH1 indicating the

development of a splay (dark blue) and crevasse (gold) system in the central to the southeastern section of the Jubilee contract area. Multiple spays are active in the central section and shows the beginning of the development of meanders of the channel complex (black line). **d** Upper section of the MH1 reservoir indicating a possible flooding surface with few dispersed sand bodies to the northern and southern section of the Jubilee contract area

with rare intervals of less mixed mudstone and interbedded mudstone and thin-bedded sandstone, that probably were deposited in large part as thin-bedded sandstone and mudstone levee-like sequences; (3) coarse-grained sandstone layers from less than 1 m to about 15 m thick, many of which coarsen and thicken upward and show sharp erosional upper contacts, that appear to represent crevasse and splay deposits. The abundance of mud-chip-rich sandstones suggests extensive erosion and downcutting through the levee or levee-like sequences; and (4) units of mainly fine-to-medium-grained turbiditic sandstone showing little or no

evidence of scour, mud-chips, or erosional tops. These may represent more distal splay deposits or flows that topped the levees without extensive erosion or crevasse formation (Figs. 23, 25, 26, 28 and 29).

At the distal section of the Jubilee basin, sediments reflect deposition on a large splay/lobe or a series of amalgamated splays/lobes by sandy high-density turbidity currents (Figs. 28 and 29). These currents included both collapsing flows and quasi-steady, largely bypassing currents that deposited thick sections of current-structured sand (Fig. 23). The surfaces of such lobes are commonly covered

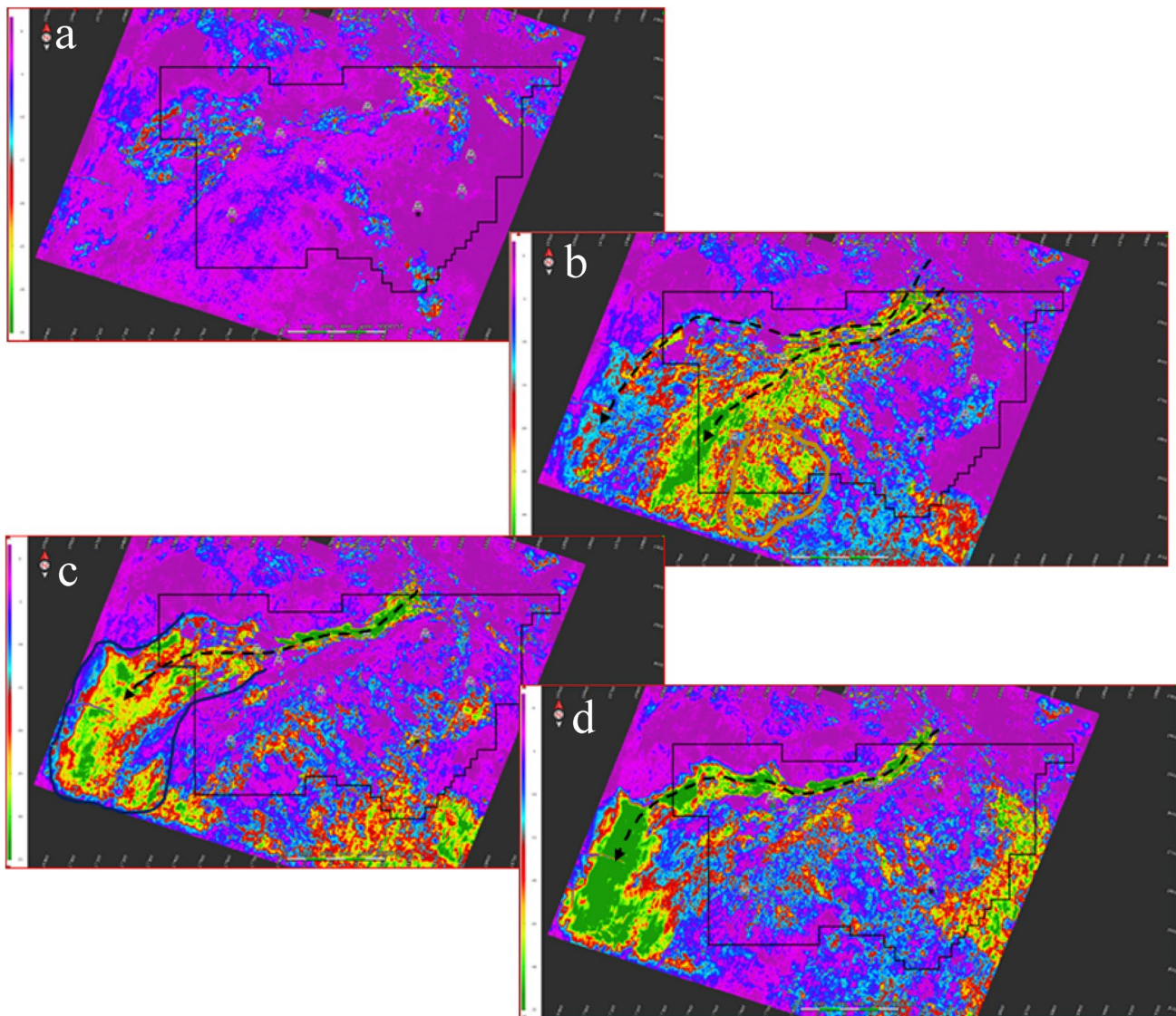


Fig. 26 Sum of Negative Amplitude (SNA) extraction showing the evolution of the complex turbidite system of the MH4 reservoir system. **a** Interval at the base of the MH4 unit marking a flooding surface with predominate mud chips from core (Fig. 21b). **b** Lower section of the reservoir unit representing the development of a south-southeast branch of the splay complex. The black arrow-line shows

the path of the channel system. **c** Interval of the upper section of the MH4 indicating the development of a single splay system to the Southwestern section of the Jubilee contract area. **d** Upper section of the MH4 reservoir indicating the well-defined southwestern splay development system

by shallow, meandering channels, but few well-defined channels can be identified (Figs. 25c and 26b). This probably reflects pervasive bed amalgamation and erosion and the shallow, non-erosive, meandering-like character of most channels. This was a large splay but probably not the terminal splay in the overall transport and depositional system.

A general model for this system is shown in Figs. 28 and 29. Flows topping the sediment source may have split into two parts (Figs. 28 and 29): (1) the near-bed high-density loads were deflected to the west, following the regional paleoslope into the Jubilee basin, and (2) the upper low-density

sediment clouds, which would have tended to continue on a more southerly course, depositing their mud, silt, and fine sand loads as the broad eastern area of sedimentation.

The Jubilee Mahogany sand depositional system is divided into several areas: flows cresting the sediment source probably moved downslope into the Jubilee basin through one or more erosional channels. These may have been strictly erosional or may have accumulated flanking levees. The W3 well was drilled in this very proximal area and did not intersect any significant channels. Upper and Lower Mahogany sediments reflect mud and mass transport

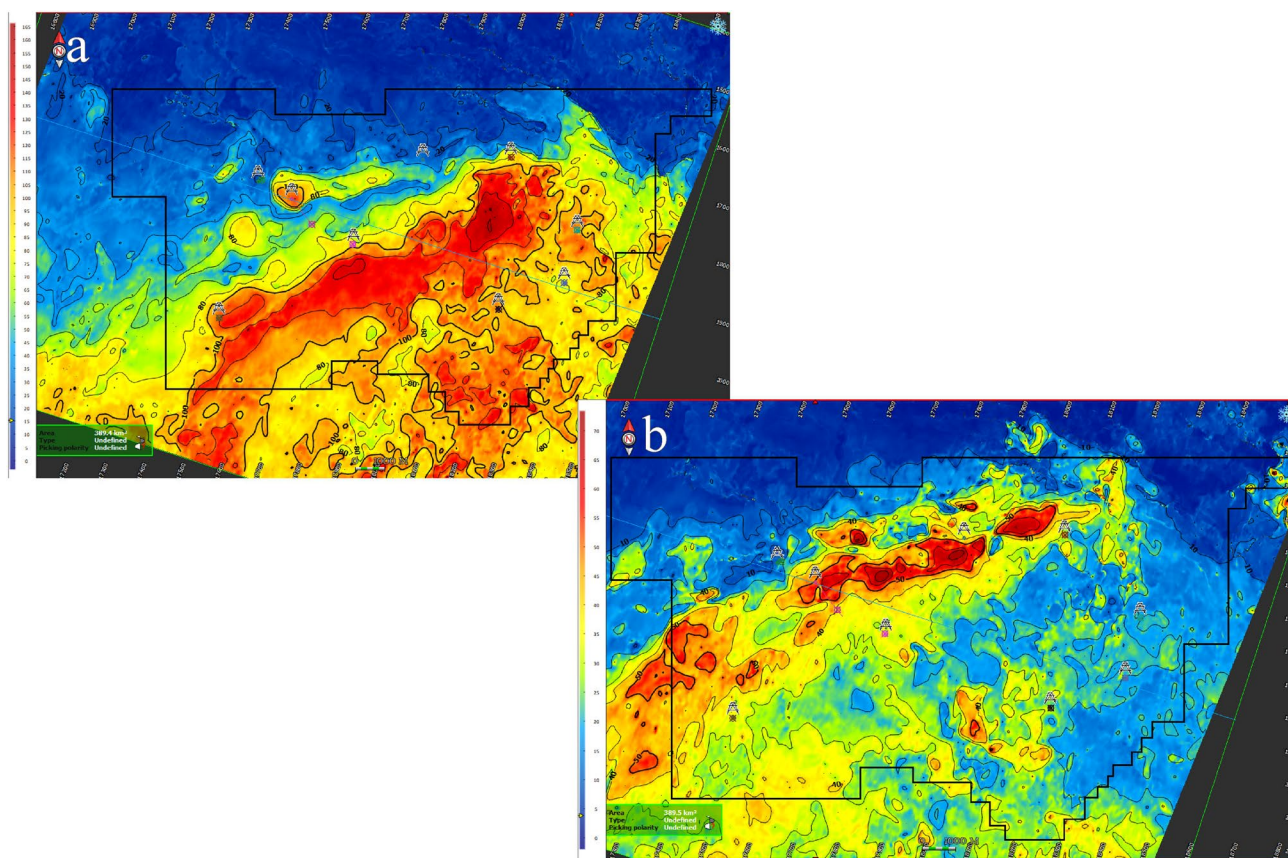


Fig. 27 Isochore (vertical depth thickness, in meters) map of the **a** MH1 reservoir and **b** MH4 reservoir unit

deposits outside of major channels and cut by numerous, mainly small erosional crevasses that fed small-to-moderate-sized splays (Figs. 28 and 29). A few sand units appear to reflect splays developed by overbanking without significant erosion. If the main channels were large areas of sediment bypassing, there may be few or no channel sand deposits preserved.

Downslope, the channels widened, shallowed, and perhaps largely disappeared (Figs. 28 and 29). The flows spread out into a broad fairway bounded on the north by the southwest slope off of the sediment source and on the southeast by the slope off of the mud- and mass-transport-covered eastern part of the Mahogany depositional area (Figs. 25, 26, 28 and 29). This fairway accumulated a series of amalgamated lobes. Sand deposition in this area may have been triggered by (1) spreading and thinning of the flows as they exited the proximal channel area, and (2) slope decrease off of the sediment source.

The distal section of the Jubilee basin represents an amalgamated splays system, reflecting largely bypassing flows (Figs. 28 and 29). This seems likely that, downslope of the splay depositional area, the flows reformed as steady or even erosive flows. Figures 28 and 29 suggest that in more distal

areas, the lobe may have been replaced by one or more channels within which the flows deposited some sand but largely bypassed areas still farther downslope.

Conclusions

The Turonian Formation is interpreted as a deep marine, marginal to a slope channel with periodic failure of levee margins and associated ingress of channel-sourced sediment into extra-channel locations as lateral crevasse splays. These were based on the recognition of seventeen sedimentary facies. Upscaling the identified lithofacies to bed-stack facies allowed the deduction of deep marine depositional environment. The identified seventeen lithofacies were grouped into six facies association depicting deep marine, bioturbated shallow marine, paludal crevasse splay and overbank sheet sand.

The cumulative frequency percentage curves and grain size statistics for Turonian sandstone are primarily indicative of the sediments' medium-grained nature. Furthermore, the majority of the sandstones have a unimodal grain-size distribution representing less variation in the

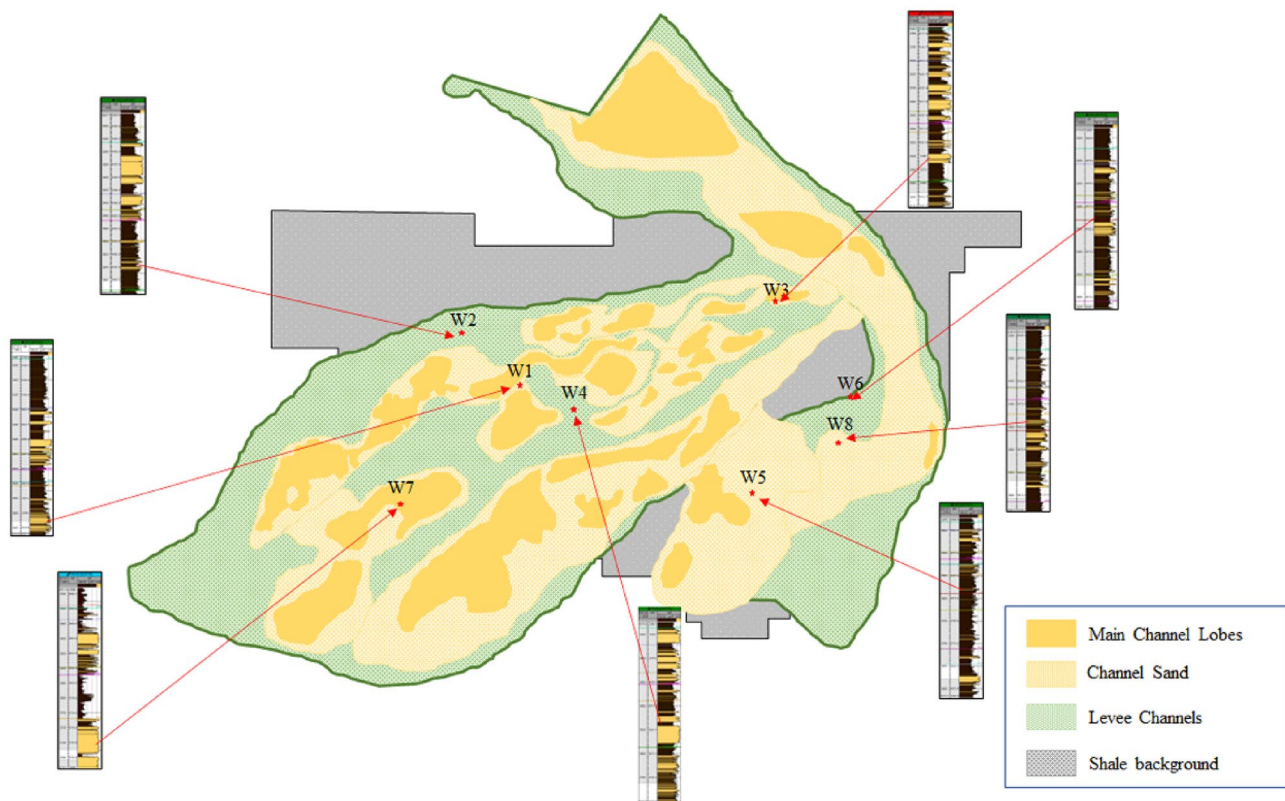


Fig. 28 Schematic representation of the key elements of the conceptual depositional model for the MH1 reservoir system

depositional processes. The sandstones have an average sorting of 2.50 (very poorly sorted) and are fine-skewed or positive skewed in nature. In general, the poorly sorted nature of the sediment depicts a blending of sediments of different sizes, resulting in an influx of kinetic energy associated with the mode of deposition in a marine environment. In most cases, both the peak and tails are poorly sorted, resulting in leptokurtic grain size patterns dominating. Linear discriminant function analyses for the Turonian sandstone are primarily indicative of turbidity current deposits in a shallow-marine environment.

In terms of diagenetic offset of the sandstone facies, syntaxial quartz overgrowths, kaolinite, and chlorite were the main authigenic phases visible in all the sandstone samples. Syntaxial quartz overgrowths appear to be volumetrically reduced in samples containing detrital clays, ferroan calcite, or abundant chlorite. These authigenic minerals resulted in reducing reservoir potential in these

samples. Minor percentages of Sa, Sb, Sf, and Sm are found in moderate reservoir quality samples. The reservoir sandstones of high quality appear to be dominated by facies types Sc, Sp, Ss, Sd, and Cgl. Overall, the majority of the sandstone samples have good reservoir quality, with permeabilities greater than 100 mD.

Our findings highlight the significance of sedimentological and facies development processes in the overall evolution of deep-water channel systems. The history of the Jubilee channel complex sets almost definitely characterizes many other emerging undersea channel systems and can be used to evaluate the distribution, shape, and structuring of the resulting reservoir sands. In turn, the Jubilee data set adds to the library of channel-levee-splay-lobe systems, serves as a prospective predictive model for hydrocarbon exploration and development, and as an outcrop explanatory analogue of a channel-splay system.

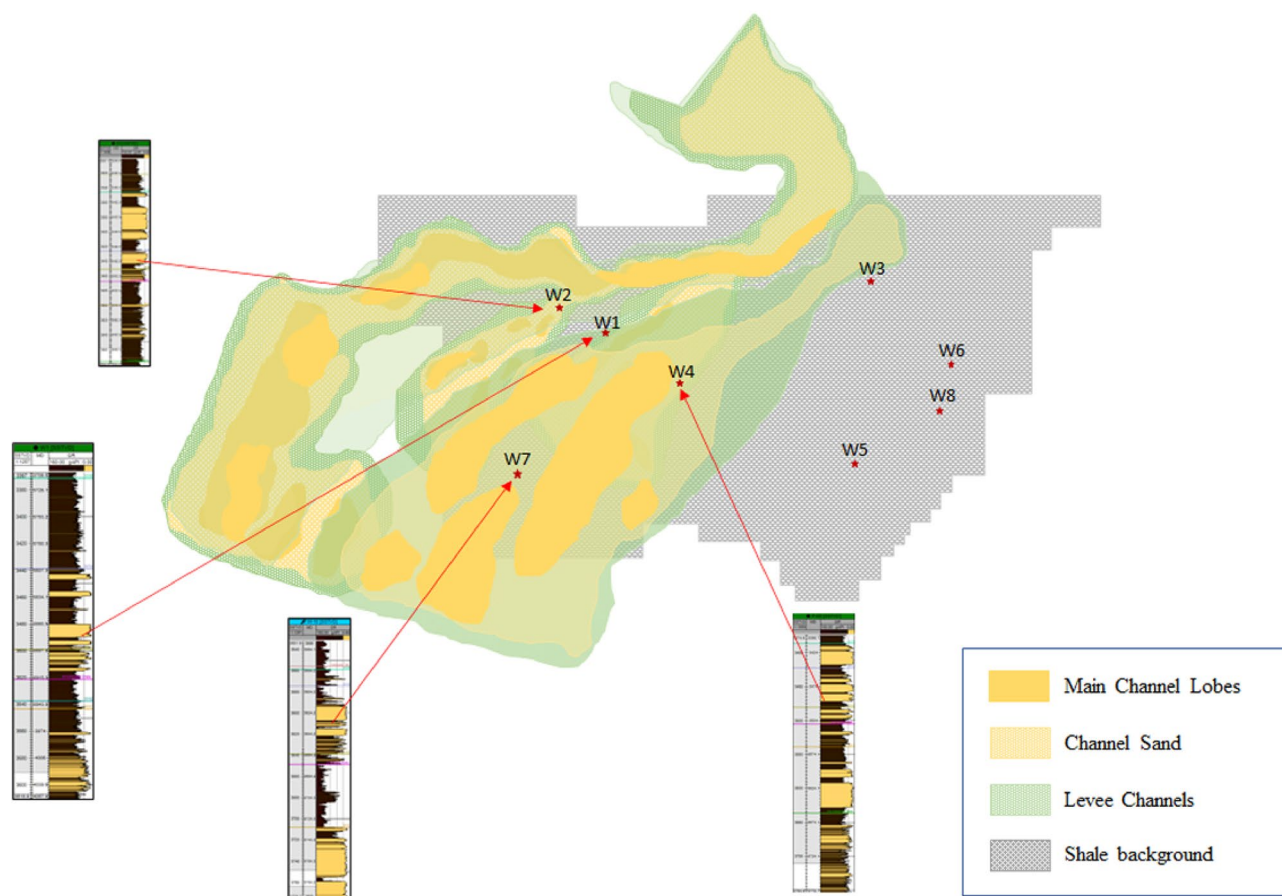


Fig. 29 Schematic representation of the key elements of the conceptual depositional model for the MH4 reservoir system

Acknowledgements We gratefully acknowledge Mr Michael Aryeetey, (Exploration and Appraisal Manager), Mr Ebenezer Apesegah (Geology Manager) and Mr Mark Prempeh (Deputy Manager) of Ghana National Petroleum Corporation for providing access to data for this research and for granting permission to publish the paper. The authors would also like to thank anonymous reviewers for their contributions to this research. Finally, we thank the University of Mines and Technology, Tarkwa, Ghana, and the Petroleum Geosciences and Engineering Department for the financial support through the Getfund Scholarship.

Author contributions EA: formal analysis, investigation, writing—original draft. AE: editing, formal analysis and supervision. ETB: editing, formal analysis and supervision. JSYK: editing, formal analysis and supervision. SAO: editing, formal analysis and supervision. BKO: editing, formal analysis and supervision. CN: editing, formal analysis and supervision.

Funding The authors received no funding for the research.

Availability of data and materials The data used for the research cannot be shared due to confidentiality agreement.

Declarations

Conflict of interest The authors declare no conflict of interest for this paper.

References

- Ahmed MJ (2021) Microfacies analysis and depositional development of Shuaiba formation in the West Qurna oil field, Southern Iraq. *Model Earth Syst Environ* 7(4):2697–2707. <https://doi.org/10.1007/s40808-020-01036-w>
- Ali SK, Janjuhah HT, Shahzad SM, Kontakiotis G, Saleem MH, Khan U, Zarkogiannis SD, Makri P, Antonarakou A (2021) Depositional sedimentary facies, stratigraphic control, paleoecological constraints, and paleogeographic reconstruction of late Permian Chhidru Formation (Western Salt Range, Pakistan). *J Mar Sci Eng* 9(12):1372. <https://doi.org/10.3390/jmse9121372>
- Al-Mimar HS, Awadh SM, Al-Yaseri AA, Yaseen ZM (2018) Sedimentary units-layering system and depositional model of the carbonate Mishrif reservoir in Rumaila oilfield, Southern Iraq. *Model Earth Syst Environ* 4(4):1449–1465. <https://doi.org/10.1007/s40808-018-0510-5>
- Antobreh AA, Faleide JI, Tsikalas F, Planke S (2009) Rift–shear architecture and tectonic development of the Ghana margin deduced from multichannel seismic reflection and potential field data. *Mar Pet Geol* 26(3):345–368. <https://doi.org/10.1016/j.marpetgeo.2008.04.005>
- Atta-Peters D, Agama CI, Asiedu DK, Apesegah E (2013) Palynology, palynofacies and palaeoenvironments of sedimentary organic matter from Bonyere-1 Well, Tano basin, Western Ghana. *Int Lett Nat Sci* 5:27–45

- Azidane H, Michel B, Bouhaddioui ME, Haddout S, Magrane B, Benmohammadi A (2021) Grain size analysis and characterization of sedimentary environment along the Atlantic Coast, Kenitra (Morocco). *Mar Georesour Geotechnol* 39(5):569–576. <https://doi.org/10.1080/1064119X.2020.1726536>
- Bempong FK, Ehinola O, Apesegah E, Hotor VK, Botwe K (2021a) Sequence Stratigraphic Framework, Depositional Settings and Hydrocarbon Prospectivity of the Campanian Section, Tano Basin Southwestern Ghana. *Petrol Coal* 63(1):204–215
- Bempong FK, Mensah CA, Bate BB, Abdul RM, Akaba PA (2021b) Seismic chronostratigraphic illustration of the Tertiary Section in Tano Basin Southwestern Ghana. *Petrol Coal* 63(3):742–750
- Bouma AH (1962) Sedimentology of some flysch deposits: a graphic approach to facies interpretation. Elsevier, Amsterdam, p 168
- Dailly P, Henderson T, Hudgens E, Kanschat K, Lowry P (2013) Exploration for Cretaceous stratigraphic traps in the Gulf of Guinea, West Africa and the discovery of the Jubilee field: a play opening discovery in the Tano Basin, Offshore Ghana. *Geol Soc Lond Spec Publ* 369(1):235–248. <https://doi.org/10.1144/SP369.12>
- Donselaar ME, Schmidt JM (2005) Integration of outcrop and borehole image logs for high-resolution facies interpretation: example from a fluvial fan in the Ebro Basin Spain. *Sedimentology* 52(5):1021–1042. <https://doi.org/10.1111/j.1365-3091.2005.00737.x>
- El-Tehiwy AA, El-Anbaawy MI, Rashwan NH (2019) Significance of core analysis and gamma-ray trends in depositional facies interpretation and reservoir evaluation of Cenomanian sequence, Alam El-Shawish East Oil Field, North Western Desert Egypt. *J King Saud Univ Sci* 31(4):1297–1310. <https://doi.org/10.1016/j.jksus.2018.12.002>
- Farrell KM, Harris WB, Mallinson DJ, Culver SJ, Riggs SR, Wehmiller JF, Moore JP, Self-Trail JM, Lautier JC (2013) Graphic logging for interpreting process-generated stratigraphic sequences and aquifer/reservoir potential: with analog shelf to shoreface examples from the Atlantic Coastal Plain Province, USA. *J Sediment Res* 83(8):723–745. <https://doi.org/10.2110/jsr.2013.52>
- Folk RL, Ward WC (1957) Brazos River bar [Texas]; a study in the significance of grain size parameters. *J Sediment Res* 27(1):3–26. <https://doi.org/10.1306/74D70646-2B21-11D7-8648000102C1865D>
- Friedman GM (1961) Distinction between dune, beach, and river sands from their textural characteristics. *J Sediment Res* 31(4):514–529. <https://doi.org/10.1306/74D70BCD-2B21-11D7-8648000102C1865D>
- Friedman GM (1967) Dynamic processes and statistical parameters compared for size frequency distribution of beach and river sands. *J Sediment Res* 37(2):327–354. <https://doi.org/10.1306/74D716CC-2B21-11D7-8648000102C1865D>
- Ghaznavi AA, Quasim MA, Ahmad AHM, Ghosh SK (2019) Granulometric and facies analysis of Middle-Upper Jurassic rocks of Ler Dome, Kachchh, western India: an attempt to reconstruct the depositional environment. *Geologos*. <https://doi.org/10.2478/logos-2019-0005>
- Huang W, Li S, Chen H, Fu C (2020) A river-dominated to tide-dominated delta transition: a depositional system case study in the Orinoco heavy oil belt, Eastern Venezuelan Basin. *Mar Pet Geol* 118:104389. <https://doi.org/10.1016/j.marpetgeo.2020.104389>
- Islam AT, Shuanghe S, Islam MA, Sultan-ul-Islam M (2017) Paleoenvironment of deposition of Miocene succession in well BK-10 of Bengal Basin using electrofacies and lithofacies modeling approaches. *Model Earth Syst Environ* 3(1):5. <https://doi.org/10.1007/s40808-017-0279-y>
- Kolla V (2007) A review of sinuous channel avulsion patterns in some major deep-sea fans and factors controlling them. *Mar Petrol Geol* 24:450–469. <https://doi.org/10.1016/j.marpetgeo.2007.01.004>
- Lowe DR (1982) Sediment gravity flows: II. Depositional models with special reference to the deposits of high-density turbidity currents. *J Sediment Petrol* 52:279–297. <https://doi.org/10.1306/212F7F31-2B24-11D7-8648000102C1865D>
- Lowe DR, Graham SA, Malkowski MA, Das B (2019) The role of avulsion and splay development in deep-water channel systems: sedimentology, architecture, and evolution of the deep-water pliocene Godavari “A” channel complex, India. *Mar Pet Geol* 105:81–99. <https://doi.org/10.1016/j.marpetgeo.2019.04.010>
- Moiola RJ, Weiser D (1968) Textural parameters; an evaluation. *J Sediment Res* 38(1):45–53
- Omisore BO, Fayemi O, Brantson ET, Jin S, Ansah E (2022) Three-dimensional anisotropy modelling and simulation of gas hydrate borehole-to-surface responses. *J Nat Gas Sci Eng* 106:104738. <https://doi.org/10.1016/j.jngse.2022.104738>
- Pacheco F, Harrison M, Chatterjee S, Ishinaga K, Ishii S, Mills W, Vargas N, Paul S, Roy P (2019) Integrated sedimentological and seismic reservoir characterization studies as inputs into a Lower Cretaceous reservoir geomodel, offshore Abu Dhabi. *First Break* 37(10):73–84. <https://doi.org/10.3997/1365-2397.2019027>
- Pattison SA (2019) Re-evaluating the sedimentology and sequence stratigraphy of classic Book Cliffs outcrops at Tusher and Thompson canyons, eastern Utah, USA: applications to correlation, modelling, and prediction in similar nearshore terrestrial to shallow marine subsurface settings worldwide. *Mar Pet Geol* 102:202–230. <https://doi.org/10.1016/j.marpetgeo.2018.12.043>
- Radwan AE (2021) Modeling the depositional environment of the sandstone reservoir in the Middle Miocene Sidri Member, Badri Field, Gulf of Suez Basin, Egypt: Integration of gamma-ray log patterns and petrographic characteristics of lithology. *Nat Resour Res* 30(1):431–449. <https://doi.org/10.1007/s11053-020-09757-6>
- Rajganapathi VC, Jitheshkumar N, Sundararajan M, Bhat KH, Velusamy S (2013) Grain size analysis and characterization of sedimentary environment along Thiruchendur coast, Tamilnadu India. *Arab J Geosci* 6(12):4717–4728. <https://doi.org/10.1007/s12517-012-0709-0>
- Rüpke LH, Schmid DW, Hartz EH, Martinsen B (2010) Basin modelling of a transform margin setting: structural, thermal and hydrocarbon evolution of the Tano Basin Ghana. *Petrol Geosci* 16(3):283–298. <https://doi.org/10.1144/1354-079309-905>
- Shahbazi A, Monfared MS, Thiruchelvam V, Fei TK, Babasafari AA (2020) Integration of knowledge-based seismic inversion and sedimentological investigations for heterogeneous reservoir. *J Asian Earth Sci* 202:104541. <https://doi.org/10.1016/j.jseaes.2020.104541>
- Shukla UK (2009) Sedimentation model of gravel-dominated alluvial piedmont fan, Ganga Plain India. *Int J Earth Sci* 98(2):443–459. <https://doi.org/10.1007/s00531-007-0261-4>
- Siddiqui NA, Ramkumar M, Rahman AHA, Mathew MJ, Santosh M, Sum CW, Menier D (2019) High resolution facies architecture and digital outcrop modeling of the Sandakan formation sandstone reservoir, Borneo: implications for reservoir characterization and flow simulation. *Geosci Front* 10(3):957–971. <https://doi.org/10.1016/j.gsf.2018.04.008>
- Siddiqui NA, Mathew MJ, Ramkumar M, Sautter B, Usman M, Rahman AHA, El-Ghali MA, Menier D, Shiqi Z, Sum CW (2020) Sedimentological characterization, petrophysical properties and reservoir quality assessment of the onshore Sandakan Formation, Borneo. *J Petrol Sci Eng* 186:106771. <https://doi.org/10.1016/j.petrol.2019.106771>
- Solórzano EJ, Buatois LA, Rodríguez WJ, Mángano MG (2021) Sedimentary facies of a tide-dominated estuary and deltaic complex in a tropical setting: the middle Miocene Oficina Formation of the Orinoco Oil Belt, Venezuela. *J S Am Earth Sci* 112:103515. <https://doi.org/10.1016/j.jsames.2021.103515>

- Spencer DW (1963) The interpretation of grain size distribution curves of clastic sediments. *J Sediment Res* 33(1):180–190. <https://doi.org/10.1306/74D70DF8-2B21-11D7-8648000102C1865D>
- Stow D, Smillie Z (2020) Distinguishing between deep-water sediment facies: turbidites, contourites and hemipelagites. *Geosciences* 10(2):68. <https://doi.org/10.3390/geosciences10020068>
- Su M, Luo K, Fang Y, Kuang Z, Yang C, Liang J, Liang C, Chen H, Lin Z, Wang C, Lei Y (2021) Grain-size characteristics of fine-grained sediments and association with gas hydrate saturation in Shenhu Area, northern South China Sea. *Ore Geol Rev* 129:103889. <https://doi.org/10.1016/j.oregeorev.2020.103889>
- Tan MT, Van Thuan D, Dy ND, Van Tao N, Ha TTT, Dao NT (2019) Environments of upper miocene sediments in the Hanoi depression interpreted from grain-size parameters Vietnam. *J Earth Sci* 41(2):182–199. <https://doi.org/10.15625/0866-7187/41/2/13798>
- Tullius DN, Leier AL, Galloway JM, Embry AF, Pedersen PK (2014) Sedimentology and stratigraphy of the Lower Cretaceous Isachsen Formation: Ellef Ringnes Island, Sverdrup Basin, Canadian Arctic Archipelago. *Mar Pet Geol* 57:135–151. <https://doi.org/10.1016/j.marpetgeo.2014.05.018>
- Xu Z, Plink-Björklund P, Wu S, Liu Z, Feng W, Zhang K, Yang Z, Zhong Y (2022) Sinuous bar fingers of digitate shallow-water deltas: Insights into their formative processes and deposits from integrating morphological and sedimentological studies with mathematical modelling. *Sedimentology* 69(2):724–749. <https://doi.org/10.1111/sed.12923>
- Boggs S (2012) Principles of sedimentology and stratigraphy
- Martinius AW, Hegner J, Kaas I, Bejarano C, Mathieu X and Mjos R (2013). Geologic reservoir characterization and evaluation of the Petrocedeno field, early Miocene Oficina Formation, Orinoco heavy oil belt, Venezuela. <https://doi.org/10.1306/13371590St643559>

Publisher's Note Springer Nature remains neutral with regard to jurisdictional claims in published maps and institutional affiliations.

Springer Nature or its licensor holds exclusive rights to this article under a publishing agreement with the author(s) or other rightsholder(s); author self-archiving of the accepted manuscript version of this article is solely governed by the terms of such publishing agreement and applicable law.